JMR EARLY CAREER SCHOLARS IN MATERIALS SCIENCE ANNUAL ISSUE: REVIEW

How to improve the stability and rate performance of lithium-ion batteries with transition metal oxide anodes

Guoyong Wang,[a] Xuning Leng, Shang Han, and Yuan Shao
Key Laboratory of Automobile Materials, Department of Materials Science and Engineering, Jilin University, Changchun 130025, People's Republic of China

Sufeng Wei
Key Laboratory of Advanced Structural Materials, Changchun University of Technology, Changchun 130012, People's Republic of China

Yan Liu[b]
Key Laboratory of Bionic Engineering (Ministry of Education), Jilin University, Changchun 130022, People's Republic of China

Jianshe Lian[c] and Qing Jiang
Key Laboratory of Automobile Materials, Department of Materials Science and Engineering, Jilin University, Changchun 130025, People's Republic of China

(Received 29 May 2016; accepted 24 August 2016)

The lithium ion battery is the most promising battery candidate to power battery electric vehicles. For these vehicles to be competitive with those powered by conventional internal combustion engines, significant improvements in battery performance are needed, especially in the energy density and power delivery capabilities. Promising substitutes for graphite as the anode material include silicon, tin, germanium, and various metal oxides that have much higher theoretical storage capacities and operated at slightly higher and safer potentials. In this critical review, metal oxides-based materials for lithium ion battery anodes are reviewed in detail together with the progress which is made in my lab on that topic. Their advantages, disadvantages, and performance in lithium ion batteries are discussed through extensive analysis of the literature, and new trends in materials development are also reviewed. Two important future research directions are proposed and performed in my lab, based on results published in the literature: the development of composite and nanostructured metal oxides to overcome the major challenge posed by the high capacity of metal oxide anodes.

Guoyong Wang

Dr. Guoyong Wang is an associate professor at Key Laboratory of Automobile Materials, Department of Materials Science and Engineering, Jilin University. Dr Wang received his BS and PhD in materials science from Jilin University in 2004 and 2009. After completing his PhD, he carried out postdoctoral research under the direction of Prof. Tong-Yi Zhang at Hong Kong University of Science and Technology for two years. His research interests focus on battery and supercapacitor materials, self-cleaning surfaces and nanocrystalline metals.

I. INTRODUCTION

Concerns over the scarcity of fossil fuels and the simultaneous greenhouse effects summon renewable energy technologies from solar, wind as well as the advent of hybrid electric vehicles (HEVs)/electric vehicles (EVs) with low emissions.[1,2] However, due to the intermittent character of renewable, reliable electrical energy storage systems are required for adapting these technologies to

Contributing Editor: Chongmin Wang
Address all correspondence to these authors.
[a]e-mail: materwanggy@jlu.edu.cn
[b]e-mail: lyyw@jlu.edu.cn
[c]e-mail: lianjs@jlu.edu.cn
DOI: 10.1557/jmr.2016.330

the demand in electricity. Among the various realistic solutions, lithium-ion batteries (LIBs), which generally have high energy density and long cycle life, are particularly adapted for applications in HEVs/EVs where a long cruising range is needed after each recharge in a short time.[3,4] Carbon-based materials are commonly used as an anode for LIBs.[5] But low theoretical capacity (372 mA h/g) is the major concern which puts sand on the wheel of its application in HEVs/EVs where a power source with high energy density and high power density is necessary.[6,7] Thus state-of-the-art LIBs can be explored only when eximious alternative electrode materials with high capacity, super rate performance, and long cycle life is found.

Transition metal oxides (TMO, M_xO_y: M = Co, Fe, Ni, Cu, Mn, etc.)[8–17] are considered as feasible anode alternatives due to the high-specific capacities induced by conversion reaction mechanism, which was first proposed and elucidated by Poizot et al.[18] However, they have relatively poor electrical conductivity and their volume change a lot during the Li^+ insertion and extraction.[19] Poor conductivity always leads to bad rate performance and low power density. Large volume change will induce pulverization which results in an insufficient lithium storage performance and a rapid capacity decay.[18] The large voltage difference between charge and discharge also results in poor energy efficiency. Thus, fabrication of high-performance transition metal oxide electrode material with good cycling stability and rate performance remains a great challenge. In this paper, I will summarize the recent progress which has been made in my lab to strengthen the morphology stability and enhance the rate performance of LIBs with transition metal oxide anodes.

II. STABILIZING THE STRUCTURE WITH THE SOLID ELECTROLYTE INTERPHASE

It is well-accepted that the solid electrolyte interphase (SEI) will form on transition metal oxide or carbonaceous anodes during the first discharge process of LIB.[20,21] Although its composition and nature is still the subject of much controversy, it has strength to some extent to support the initial morphology contrary to the pulverization.[22] Recently, ultrathin mesoporous $NiCo_2O_4$ nanosheets were directly grown on Ni foams in my lab to form an efficient and reversible anode for lithium-ion half-cell batteries.[23] The morphology can be seen in Fig. 1. They are interconnected to build up a honeycomb-like architecture which offers a large electrolyte contact area and good structure integrity. The ultrathin thickness of the sheet is also beneficial for the fast Li ion reaction and diffusion in the electrode. The nanosheets in fact are monolayers of 10 nm $NiCo_2O_4$ nanoparticles, as proved by the TEM image shown in Fig. 2. Such structure suggests a weak strength of the sheet. But during the first discharging, the SEI film is formed on it. The SEI film combined with the honeycomb-like architecture endows the electrode a good

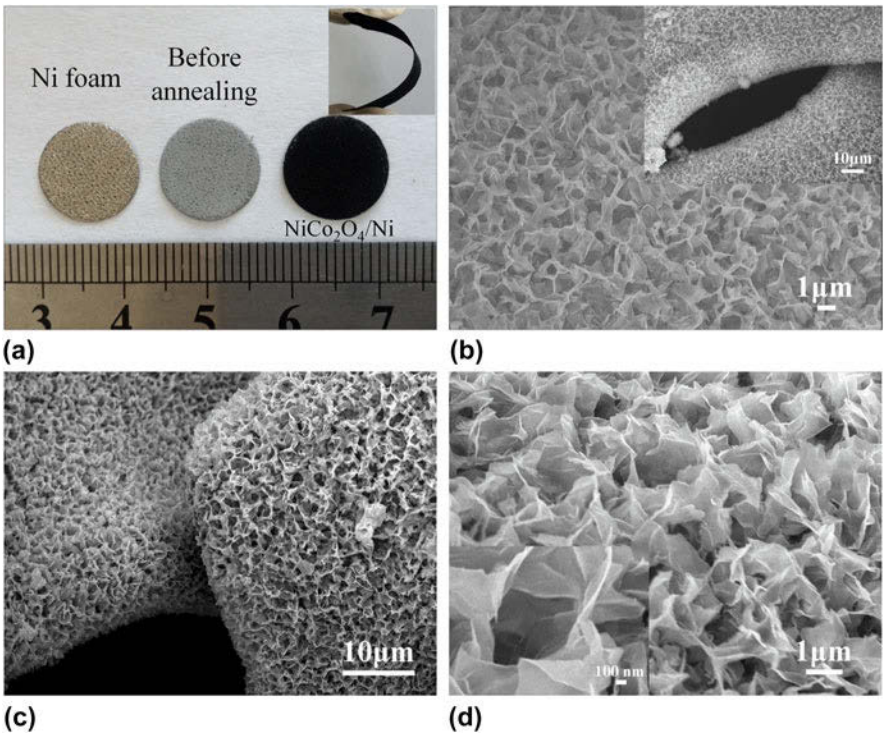

FIG. 1. (a) Pictures of the Ni foam before and after the annealing of $NiCo_2O_4$/Ni, and the inset is the photograph of a flexible $NiCo_2O_4$/Ni before punching; (b) SEM image of the Ni foam before the annealing of $NiCo_2O_4$/Ni; (c) low-magnification SEM image of $NiCo_2O_4$/Ni after annealing; (d) high-magnification SEM image of $NiCo_2O_4$/Ni after annealing and the inset is partial enlarged detail.

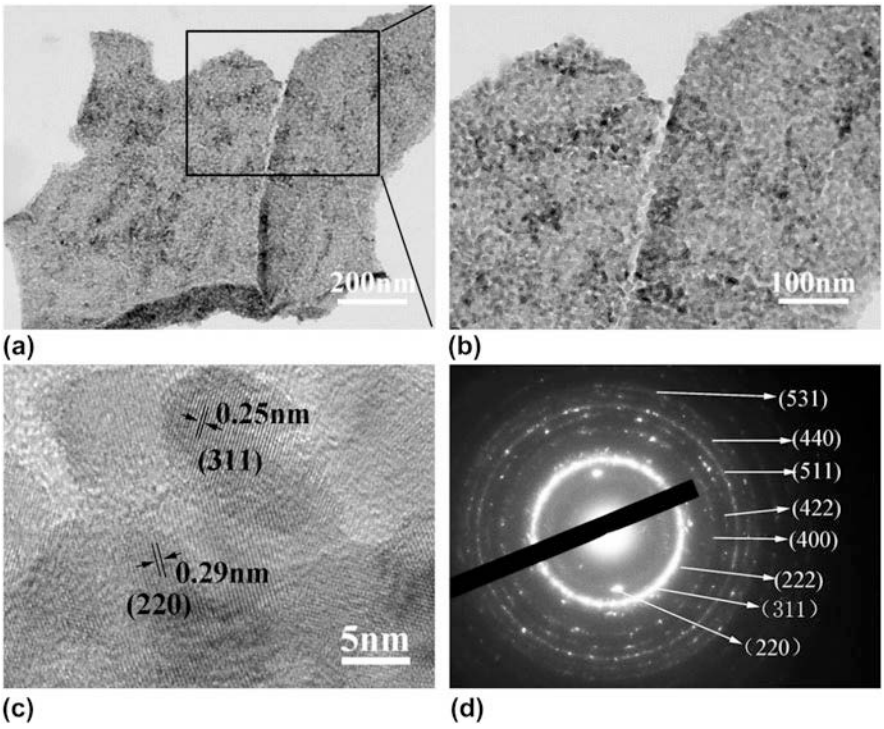

FIG. 2. (a and b) TEM image; (c) HRTEM image; (d) SAED pattern of the $NiCo_2O_4$ nanosheet scratched from Ni foam.

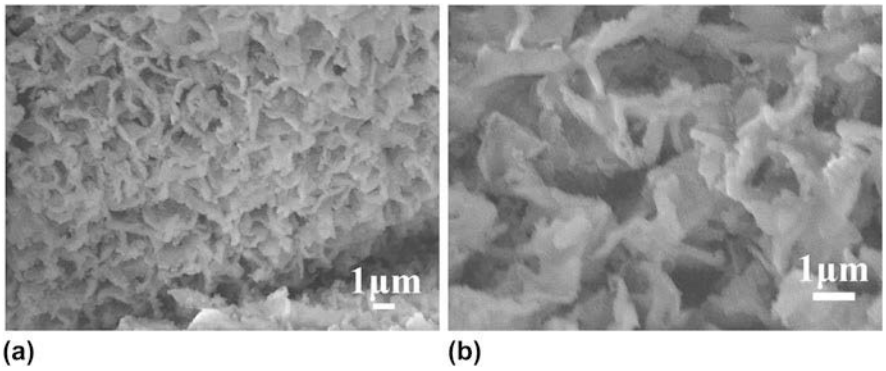

FIG. 3. SEM images of the $NiCo_2O_4$/Ni foam electrode after 50 cycles.

cyclic stability. As shown in Fig. 3, after 50 cycles the initial honeycomb-like architecture is pretty reserved. Thus, the electrode made by such architecture has pretty well Li ion storage performance. The electrochemical investigation of the electrode is show in Fig. 4. For the CV curves of Fig. 4(a), the dominant cathodic peak locating at around 0.67 V for the first cathodic sweep shifts to 0.93 V with reduced intensity in the subsequent scans, which indicates the irreversible processes to form the SEI film during the first cycle.[9] The subsequent cycles following the first cycle overlap very well. So the SEI is very stable, which guarantees a good reversibility of the electrochemical reaction. As shown in Fig. 4(b), the initial discharge and charge capacities of the electrode are 1738 and 1244 mA h/g, respectively. The large irreversible capacity loss in the first cycle should be associated with the SEI film formation. The $NiCo_2O_4$/Ni foam electrode has a much better cycle performance than the pasted $NiCo_2O_4$ powders electrode, as shown in Fig. 4(c). It exhibits remarkable capacity retention (1170.1 mA h/g in the 50th cycle) upon prolonged cycling with a high coulombic efficiency of nearly 99%, which is even higher than the theoretical capacity of $NiCo_2O_4$ (980 mA h/g). As shown in Fig. 4(d), the $NiCo_2O_4$/Ni foam electrode delivers average discharge capacities of 1343.1, 1241.5, 974.4, 780.2, and 398.2 mA h/g at current densities of 0.2, 0.5, 1.0, 2.0, and 4.0C, respectively. Importantly, a high capacity of 1101.2 mA h/g can be recovered when the current density is reduced back to 0.2C.

The enhanced charge transfer efficiency and improved electrical conductivity of the $NiCo_2O_4$ electrode can be investigated by the comparison of the Nyquist plots as measured by electrochemical impedance spectroscopy (EIS), which shows the usual feature of energy device: an inclined straight line in the low-frequency region and a semicircle in the high-frequency region (Fig. 5). Apparently, the initial diameter of the semicircle for $NiCo_2O_4$/Ni foam electrode is much smaller than the pasted electrode. After 50 cycles, both semicircles have enlarged diameters. But the semicircle diameter for the pasted electrode enlarged even more. Thus the unique structure of $NiCo_2O_4$/Ni endows the electrode much lower contact and charge-transfer impedances.

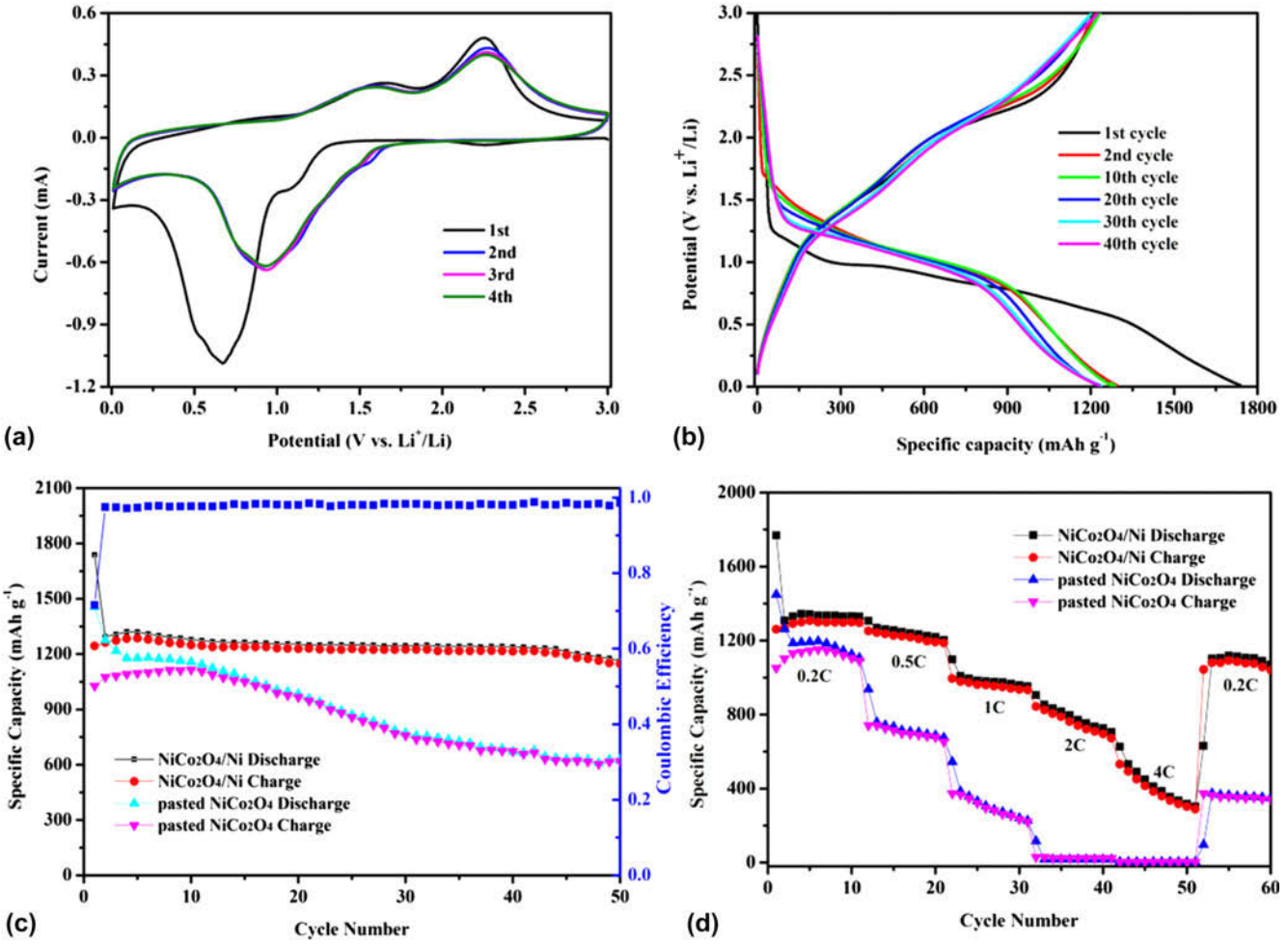

FIG. 4. (a) CV curves of the $NiCo_2O_4$/Ni electrode at a scan speed of 0.2 mV/s in the voltage window of 0.01–3 V; (b) discharge–charge curves of the $NiCo_2O_4$/Ni electrode at a current density of 0.2C; (c) cycle performance of $NiCo_2O_4$/Ni foam and pasted $NiCo_2O_4$ electrode at 0.2C, and the coulombic efficiency of $NiCo_2O_4$/Ni foam; (d) rate capabilities of the $NiCo_2O_4$/Ni foam and pasted $NiCo_2O_4$ electrode cycled at different current rates from 0.2 to 4C. (1C = 1 A/g).

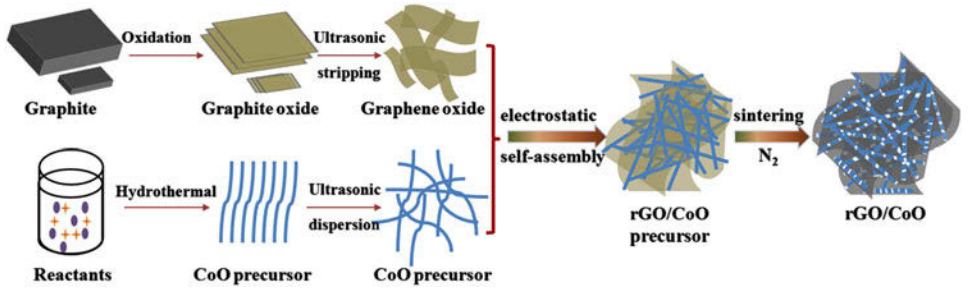

FIG. 5. Nyquist plots of $NiCo_2O_4$/Ni foam electrode and pasted $NiCo_2O_4$ powder electrode for the 1st and 50th cycles.

As long as the unique structure is reserved, the good electrochemical performance can be retained. The morphology of the $NiCo_2O_4$/Ni electrode after 50 cycles was observed by SEM, and the image is shown in Fig. 3. The honeycomb-like structure is perfectly reserved, although the sheet thickness changed to around 200 nm. The increase of the sheet thickness should be relative to the covering of thick SEI film forming during the first discharge process and the film is conducive to maintain structural integrity.[24] The good electrochemical performance of the $NiCo_2O_4$/Ni electrode should be related to its unique features. First, the nanosheets were directly grown on the current collector, which guarantees a good mechanical adhesion. Thus, the electrode doesn't suffer a fast capacity fading as abscission of the electrochemical active materials. Meanwhile the close contact provides a fast pathway for charge-transfer, which induces low contact and charge-transfer impedances. Second, the honeycomb-like architecture constructed by ultrathin mesoporous nanosheets provides huge pathway for electrolyte and Li^+ diffusion and markedly increases the amount of contact areas between active materials and electrolyte. It can make Li^+ diffusion to reaction site much easier and greatly reduce the reaction and Li^+ diffusion impedance. Third, the open 3D honeycomb-like architecture provides sufficient space to buffer the volume changes during the charge/discharge process.[24] In this architecture, the nanosheets will support each other, which should enhance the integrity of the structure. On the contrary, the pasted electrode cannot ensure the direct contact between the active material and current collector or sustain the quality of the adhesion because the conductive additive and binder would be subjected to periodical variations in the volume and strain of the active material.[25] The random and unordered stacking of the nanosheets could block the Li^+ diffusion pathways. The presence of binder can also impede electron conduction.[26]

III. STABILIZING TMO WITH REDUCED GRAPHENE OXIDE

Graphene, as a monolayer of carbon atoms arranged in a honeycombed network of six-membered rings, has triggered a gold rush since its discovery. Its good mechanical properties, high theoretical surface area of 2630 m^2/g, good electronic conductivity suggest it would have a bright prospect in LIBs. What is more, it has high theoretical lithium storage of 744 mA h/g.[27,28] Thus, graphene can support another advanced anode materials meanwhile it also can act as a pathway for the flow of electrons from the active material to current collector.[29–31] Up to now, many nanoparticles (NPs) M_xO_y/graphene composites have been investigated as LIB anode materials, such as SnO_2/graphene,[32–34] Mn_3O_4/graphene,[35] CuO/graphene,[36] and Fe_2O_3/graphene.[37] They usually exhibit much better electrochemical performance than their bare counterparts. However, the NPs are still prone to aggregate during cycling because of nonintimate/tight contact between the NPs and graphene sheets (GS) layers.[8,38] On the other hand, the overlapping of GS during electrode preparation and electrochemical test is also a critical problem, which may result in inadequate adhibition of graphene. Therefore, to adequately utilize the unique properties of individual GS and fully harness the synergistic effect between GS and M_xO_y, the main challenges in the synthesis of graphene/M_xO_y composites lie in how to effectively enhance the contact between GS and M_xO_y and inhibit too much overlapping and agglomeration of GS.

Recently, a rGO/CoO composite anode with high specific capacity, good cycling stability and excellent rate capability was synthesized in my lab.[39] The preparing procedure of rGO/CoO nanowires mutually-supporting porous structure is illustrated in Fig. 6. Uniform and well-crystalline $Co(CO_3)_{0.5}(OH)\cdot 0.11H_2O$ nanowires, served as CoO precursor, were firstly fabricated via a glycol-assisted hydrothermal method. Then the positively charged nanowires were attached to negatively charged GO sheets because of electrostatic interaction. As the composites were sintered in nitrogen atmosphere, the CoO precursor and GO nanosheets were thermally in situ decomposed to CoO nanowire and rGO. Eventually, a unique self-assembled rGO/CoO nanowires mutually-supporting porous structure was successfully prepared. The in situ direct generation of rGO/CoO composites by one-step thermal treatment ensures a strong interaction and better structural stability. The morphology of the CoO precursor and its evolution after annealing were detected by SEM and the images are shown in Fig. 7(a) and 7(b). The pristine precursor is nanowire with a diameter of 15–25 nm and length of several micrometers. The wire surface is smooth and flat. After annealing, the wire

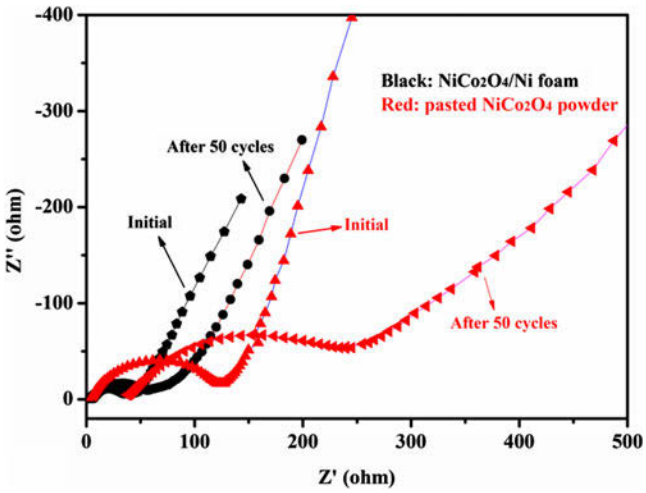

FIG. 6. Schematic illustration of the procedures for preparation of rGO/CoO nanowires mutually-supporting porous structure.

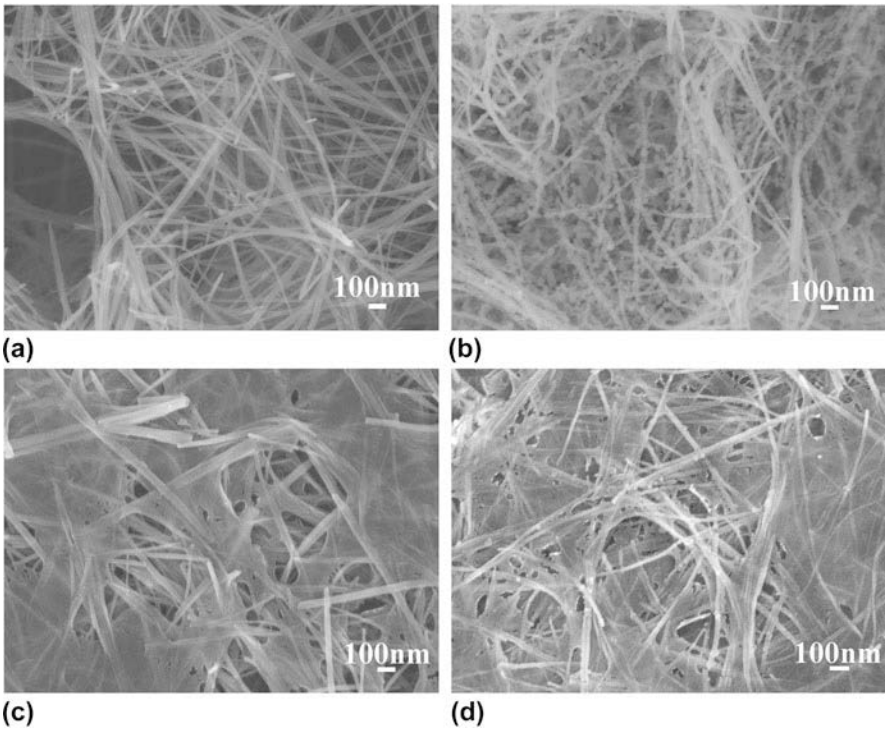

FIG. 7. FESEM images of (a) CoO precursor nanowires; (b) CoO after annealing; (c) GO/CoO precursor by electrostatic interaction; (d) rGO/CoO after annealing.

changed to a dot-line, a sequence of NPs with a diameter of about 10–20 nm. The effect of rGO on the morphology evolution of the wire was also investigated by SEM. The images are shown in Figs. 6(c) and 6(d) which can be compared to Figs. 7(a) and 7(b). The adding of GO doesn't affect the morphology of the wire, as shown in Fig. 6(c). $Co(CO_3)_{0.5}(OH)\cdot 0.11H_2O$ nanowires are uniformly adsorbed on GO nanosheets, and both of them supported each other. Thus a 3D loose network system with lots of voids is formed by them. As shown in Fig. 7(d), the annealing has very less effect on the morphology of the system. The wire is still long and smooth and the sheet is still large and flat. It doesn't show a similar view like the image in Fig. 7(b). A similar phenomenon was also observed by TEM. After annealing, the wire changed to a sequence of NPs of about 10–20 nm as shown in Fig. 8(a). And the wire retained its morphology by the help of rGO after annealing as proved by the image of Fig. 8(b). In fact, the line still consisted of similar size nanocrystals as proved by the image of Fig. 8(c). It seems like a line because these nanocrystals link with each other firmly. The grain boundary between vicinal crystals can be clearly detected by the HRTEM image shown in Fig. 8(d). The morphology characterization by SEM and TEM revealed that the CoO wires were firmly anchored on the rGO surface. So the integrity of the wires was retained even after annealing. Meanwhile the existence of the wires between rGO sheets is also effective to inhibit the restacking of rGO sheets.

The cycle performance of the rGO/CoO electrode was tested at a current density of 0.1 A/g, and it was compared with the pure CoO electrode. The results are shown in Fig. 9(a). The capacity of the rGO/CoO is superior to the CoO at the initial cycle. The reversible capacities are gradually increasing in the first dozens of cycles, which may be attributed to the formation of a polymeric surface film attached to the active material.[27] It gets a maximum value of 1027 mA h/g at the 36th cycle, which is about 99.5% of the initial discharge capacity, and it can still maintain 994 mA h/g even after 100 cycles. The value is even higher than the theoretical value of rGO/CoO composite ($C_{\text{theoretical}} = C_{\text{CoO}} \times$ mass percentage of CoO + $C_{\text{graphene}} \times$ mass percentage of graphene = $716 \times 92\% + 744 \times 8\% = 718.2$ mA h/g). Such high specific capacity of rGO/CoO should be attributed to the following points: firstly, the rGO sheets have numerous significant disorder and defects, which can also contribute to the lithium storage capacity, except for the inherent capacity (formation of intercalation compounds Li_3C).[27,40] Secondly, the reversible decomposition of the electrolyte with the formation of SEI and extra lithium-ion adsorption/desorption on the SEI during cycling may also lead to the high experimental lithium storage capacity.[18,41] For the pure CoO electrode, the initial capacity only is maintained for 18 cycles. After that, it declines sharply from 708 to 506 mA h/g.

The rGO/CoO electrode also exhibits excellent rate performance. As shown in Fig. 9(b), the rate performance

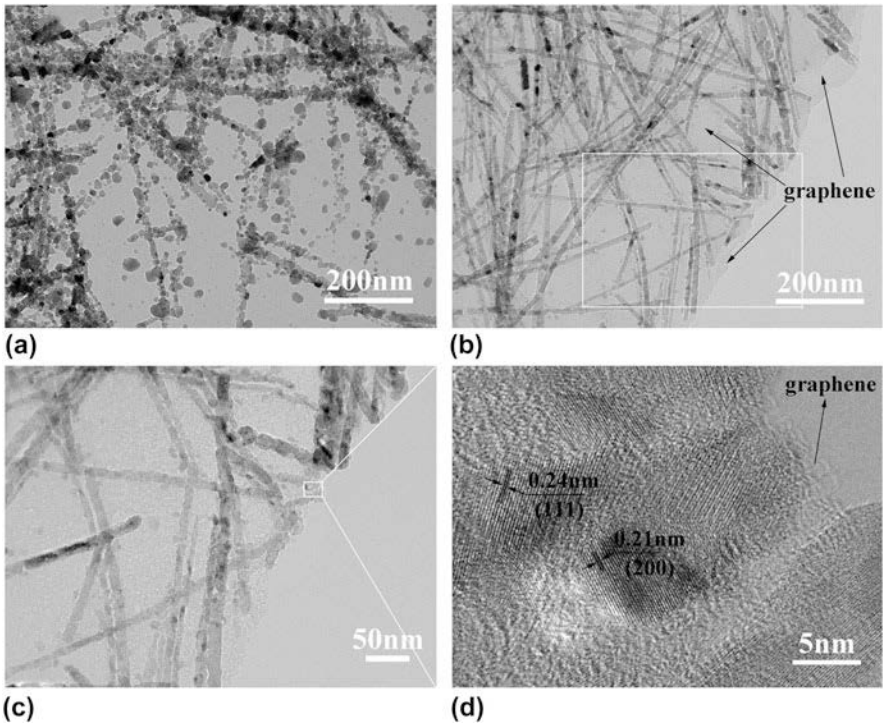

FIG. 8. (a) TEM image of the pure CoO; (b and c) TEM and (d) HRTEM images of the rGO/CoO. The distance of two interference fringes was measured to be 0.24 and 0.21 nm, respectively, which is equal to the interplanar spacing of (111) and (200) plane of cubic CoO according to JCPDS 43-1004 XRD card.

was compared with the CoO electrode. The electrode delivers average reversible capacities of 960, 846, 790, 718, 646, 577, 504, 388, and 262 mA h/g for 0.1, 0.2, 0.4, 0.8, 1.6, 3.2, 5.0, 7.0, and 10C, respectively. It means 28% capacity is retained even after the current density enlarged 100 times from 0.1C to 10C. As the current rate returns to 0.1C, the initial capacity is reserved. The curve even persist the increasing trend during 72–82 cycles and 102–108 cycles, just same like the trend in first 11 cycles. Finally, the capacity rises above 1046 mA h/g at the 112th cycle, which is very close to the initial discharge capacity (1068 mA h/g). However, as the current density increase from 0.1 to 5C, the specific capacity of the CoO electrode decreases sharply to only 7.6% of its initial capacity. As the current density increases even higher up to 10C, the specific capacity is close to zero. When the current density returns to 0.1C, the electrode can't regain its initial capacity yet. Only 60% capacity is recovered. In fact, the cycle performance of the rGO/CoO electrode is much better than 100 cycles. As shown in Fig. 9(c), the electrode can maintain a reversible capacity of 790 mA h/g at a current rate of 1C to the 130th cycle. Then it suffers a sharp fading to 530 mA h/g from the 130th cycle to the 180th cycle. After that, the capacity levels off above 610 mA h/g until the 620th cycle with a coulombic efficiency of around 98.3–100.4%. At a higher current density of 3C, the trend is similar to 1C, but the specific capacity still can maintain 520 mA h/g even after 750 cycles. The reasons for the obvious capacity decreases at high rates maybe as follows[42–44]: (i) the continuous reduction of active materials due to the insetting of metal Co in Li_2O matrix partially, especially it occurs at high rates; (ii) the brush-fire aggregation of the active materials to larger clusters cannot be completely avoided; (iii) the structure strain of the active materials can't be totally eliminated during cycling even though the voids and rGO sheets could accommodate the volume change of the active species. These measurements confirm the merits of the rGO/CoO electrode.

To clarify the difference of the electrochemical performances, EIS measurements are also carried out at frequencies from 100 kHz to 0.01 Hz on both electrodes before test and after 100 cycles at 0.1C to uncover the electrode kinetics evolution and its relationship to electrochemical performance (Fig. 10). The Nyquist plots could be well fit by using a commonly adopted equivalent circuit (the inset of Fig. 10).[45–47] In the equivalent circuit, R_e is the electrolyte resistance; R_{ct} is the charge-transfer resistance; Z_w is the Warburg impedance related to the diffusion of Li ions into the bulk electrodes, and CPE is the constant phase-angle element, involving double layer capacitance. Whether the EIS was tested initially or after 100 cycles, the charge-transfer resistance (R_{ct}) for the rGO/CoO composite is much smaller than the CoO electrode. This indicates that the rGO/CoO composite electrode possess lower charge-transfer impedances, which

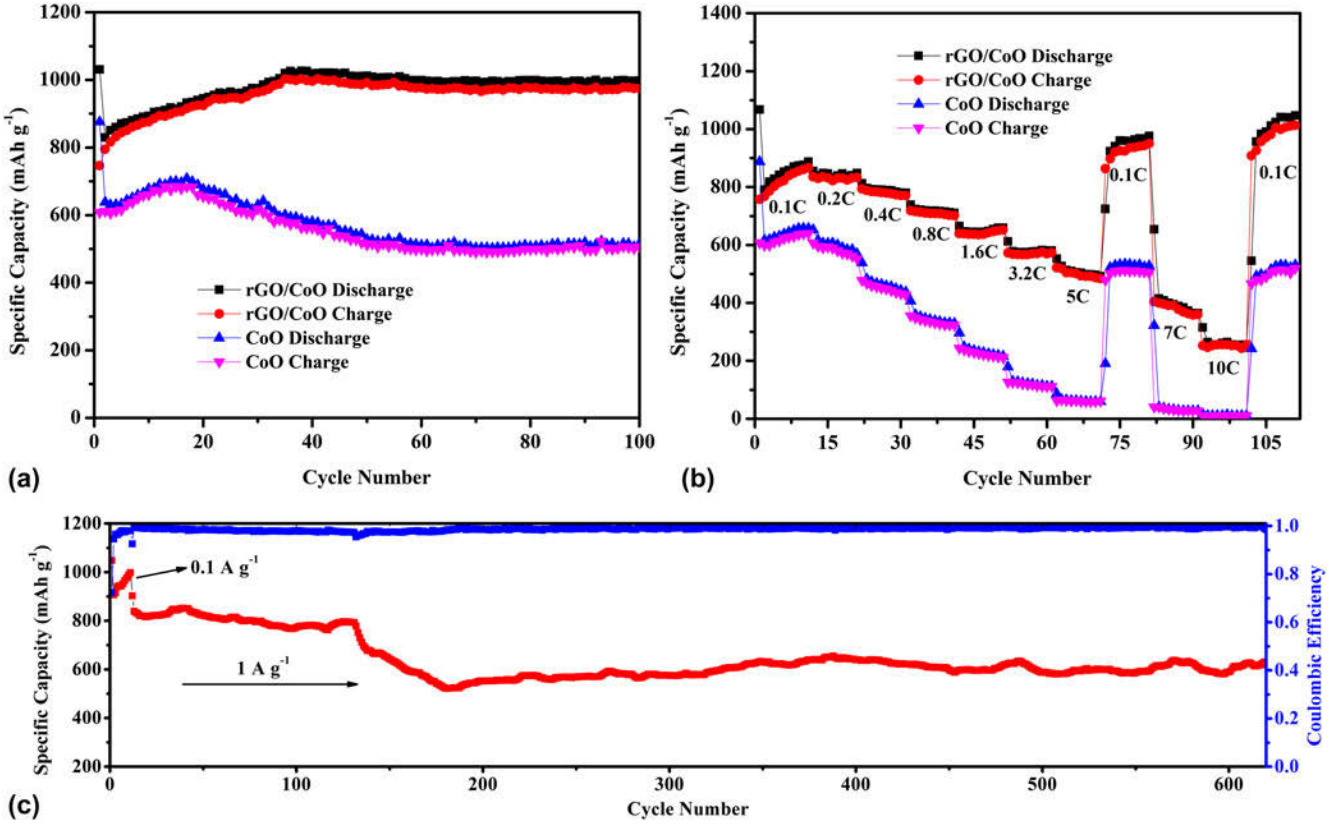

FIG. 9. (a) Charge/discharge capacities of the CoO and rGO/CoO electrode at a current density of 0.1C; (b) rate capabilities and cycle performance of the CoO and rGO/CoO electrode cycled at different current rates from 0.1 to 10C; (c) cycle performance and coulombic efficiency for rGO/CoO electrode at higher current density of 1C (for the first 10 cycles at 0.1C, 1C = 1 A/g).

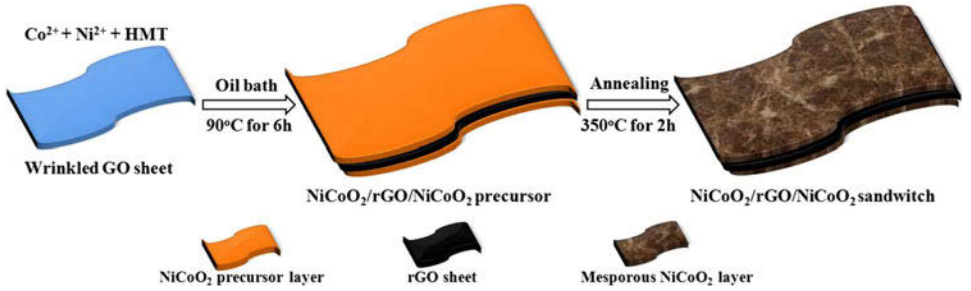

FIG. 10. Nyquist plots (solid dots) for the cells made of CoO and rGO/CoO electrodes and the fit curves (solid lines) using the equivalent circuit shown in the inset.

can lead to rapid electron transport during lithiation/delithiation process and thus result in significant improvement on the rate performance. The tail for the rGO/CoO electrode at low frequency has higher slope than the CoO electrode, which indicates that the rGO/CoO electrode possesses lower lithium diffusion impedance.[48] The impedances both increased after 100 cycles, which may be attributed to the formation of SEI film.[49–51] But such increase in impedance does not lead the decline of capacity.

The excellent electrochemical performance of the rGO/CoO anode should be ascribed to the unique structure it has.[52–54] In this experiment, the attachment was completed before the annealing which induce the conversion of CoO precursor nanowires and GO sheets to rGO. The procedure is obviously effective to enhance the adhesion force between CoO nanowire and rGO. The CoO nanowires in fact are tightly anchored on the rGO sheets, so the integrity of the nanowires is kept. The rGO/CoO electrode can possess an outstanding electronic conductivity to rGO benefiting from the good adhesion. And rGO sheets are able to act as an expressway for charge transfer. The conductivity of the electrode is improved. Secondly, CoO nanowires are firmly anchored on rGO sheets surface. The CoO NPs which constitute the nanowire have little chance to shed and aggregate. Meanwhile the rGO which is separated by the CoO

nanowires also have little chance to restack. Thus, the voids between the network of the CoO wires and rGO can be reserved. The voids and the interstices in the wire formed during gas releasing are essential for high performance transition metal oxide electrode for they supply uniform interspaces to accommodate the large volume change the transition metal oxide electrode suffers during lithiation/delithiation. The cycle performance of the electrode can be improved. Finally, the voids and interstices, together with rGO sheets, can also supply a large interface and pathway for Li^+ reaction and diffusion. The nanowires, NPs indeed, with small diameter heavily shorten the hard pathway for Li^+ diffusion inside transition metal oxide. Li^+ diffusion rate in the cell assembled by the rGO/CoO electrode is improved, which induce the excellent rate performance.

In another way, rGO sheets can also be encapsulated by TMO materials to form advanced LIB anodic materials. A facile and scalable strategy is proposed in my recent work for synthesis of a unique porous architecture built by ultrathin wrinkled $NiCoO_2$/rGO/$NiCoO_2$ sandwich nanosheets. Ultra-hydrophilic graphene oxide (GO) sheets are dispersed into Ni^{2+} and Co^{2+} solution as template for $NiCoO_2$ precipitation. GO surface has ample oxygenic functional groups, some of which are negative polar.[39,55] They can absorb and anchor positive ion such as Ni^{2+} and Co^{2+} on both sides of GO sheets.[16,56] Ni^{2+} and Co^{2+} co-precipitate as $NiCoO_2$ precursor layers on GO sheet, that is simultaneously chemically converted to reduced GO (rGO) by HCHO, as enough NH_3 and HCHO are formed by hydrolyzing hexamethylenetetramine. Then $NiCoO_2$/rGO/$NiCoO_2$ sandwich nanosheets can be obtained by annealing. The sandwich sheets are as ultrathin as GO, thus they are random wrinkled. As these random wrinkled sheets stack together during drying, they mutually brace each other to form a unique porous architecture. This architecture owns sufficient specific surface area to facilitate the interaction of the active materials with electrolyte.[57] In the architecture, the poor conductivity of $NiCoO_2$ is heavily improved by high quality rGO, meanwhile the perfect flexibility of rGO can also guarantee the stability of the architecture. The electrochemical tests on the $NiCoO_2$/rGO/$NiCoO_2$ composite validate the architecture owns big advantage as electrode materials in SCs and LIBs.

The synthetic process of $NiCoO_2$/rGO/$NiCoO_2$ sandwich nanosheet is schematically illustrated in Fig. 11.[58] Firstly, GO sheets are dispersed into de-ionized water, and then Ni^{2+}, Co^{2+} and HMT are added in the solution serially. The metal cations (Ni^{2+} and Co^{2+}) could be strongly absorbed by the polar oxygen-containing functional groups, such as hydroxyl and carboxyl, on both sides of GO sheets.[59] As the solution is heated to 90 °C, the HMT starts to hydrolyze into HCHO and NH_3. The former, as a strong reducing agent, has ability to

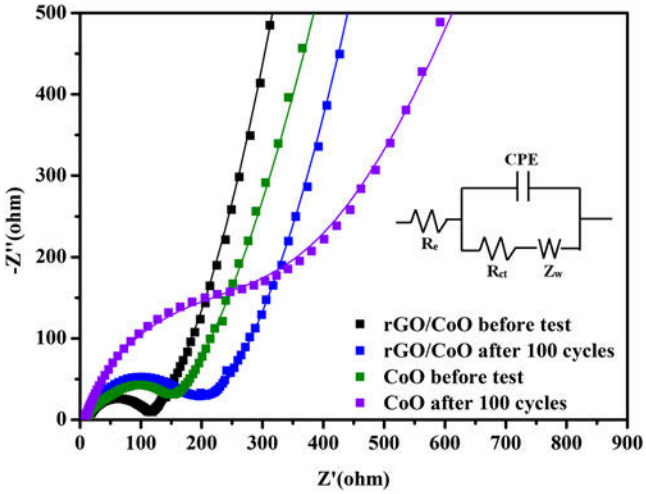

FIG. 11. Schematic illustration of the synthesis of the wrinkled ultrathin $NiCoO_2$/rGO/$NiCoO_2$ sandwich nanosheets.

reduce GO into graphene, and the latter can cause the increase of the solution pH value, and the precipitation of the $NiCoO_2$ precursor.[60] During the reaction, $NiCoO_2$ precursors prefer to nucleate on the surface of GO sheets because of the coordination effect between metal cations and oxygen-containing functional groups of GO.[56] Simultaneously, GO sheets are chemically reduced via losing oxygen-containing surface groups because of the presence of strong reducing agent (HCHO). As a consequence, ultrathin $NiCoO_2$ precursor layers are generated on both sides of rGO sheets (designed as $NiCoO_2$/rGO/$NiCoO_2$ precursor). Finally, the $NiCoO_2$/rGO/$NiCoO_2$ sandwich nanosheets can be obtained by annealing treatment in N_2. The whole formation reactions of $NiCoO_2$ could be described by the following steps:

$$(CH_2)_6N_4 + 6H_2O \rightarrow 6HCHO + 4NH_3 \quad , \qquad (1)$$

$$H_2O + NH_3 \rightarrow NH_4{}^+ + OH^- \quad , \qquad (2)$$

$$Co^{2+} + Ni^{2+} + 4OH^- \rightarrow Co(OH)_2 + Ni(OH)_2 \quad , \qquad (3)$$

$$Co(OH)_2 + Ni(OH)_2 \rightarrow NiCoO_2 + 2H_2O \quad . \qquad (4)$$

The structure and morphology of the as-prepared samples were characterized by FESEM and TEM. Figures 12(a) and 12(b) show the FESEM and TEM images of the pure $NiCoO_2$ sheets. The $NiCoO_2$ sheets are ultrathin, leading to the faint mass-density contrast in TEM image, and the thickness determined from the FESEM image is about 10 nm. The selected-area electron diffraction (SAED) pattern [the inset of Fig. 12(b)] shows well-defined diffraction rings, indicating the crystalline nature of the cubic phase. Although the sheets are crystalline, as validated by

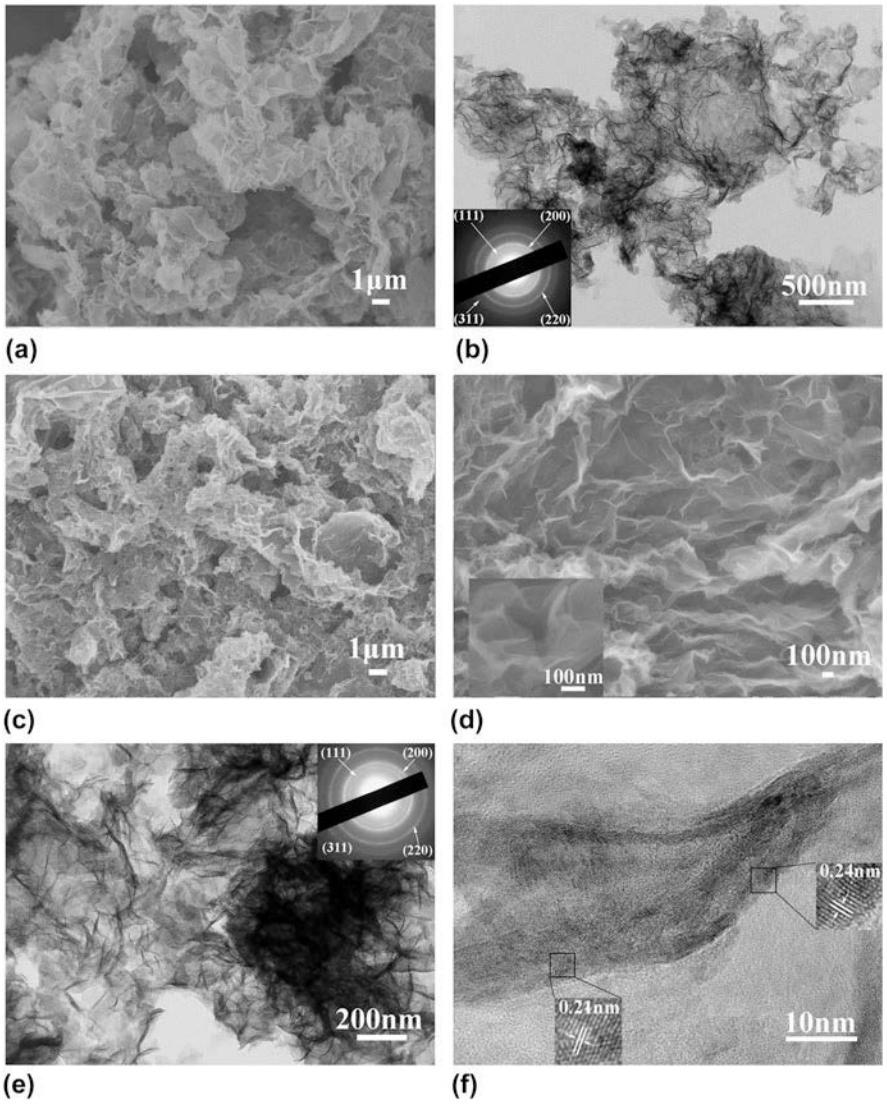

FIG. 12. (a) SEM image and (b) TEM image of the pure $NiCoO_2$ and the inset is the corresponding SAED pattern; (c) and (d) SEM images of the $NiCoO_2$/rGO/$NiCoO_2$ composite; (e) TEM image and (f) HRTEM of the $NiCoO_2$/rGO/$NiCoO_2$ composite. The inset in e is the corresponding SAED pattern.

the XRD result and SAED pattern, they still have lots of random wrinkles, as shown in the FESEM and TEM images, because of ultrathin thickness. As the randomly wrinkled sheets were assembled together, they inevitably composed a unique porous framework shown in Fig. 12(a). The as-prepared $NiCoO_2$/rGO/$NiCoO_2$ composite has a similar structure, as shown by the FESEM images in Figs. 12(c) and 12(d) and the TEM image in Fig. 10(e). The diffraction rings of corresponding SAED pattern in the inset of Fig. 12(e) and the interference fringe in the HRTEM image of Fig. 10(f) validate that crystalline $NiCoO_2$ sheets formed on the rGO sheets. After two $NiCoO_2$ sheets anchor on both sides of GO, the thickness of the sandwich sheet is about 6 nm which is also determined by AFM. After adding GO, the thickness of the synthesized $NiCoO_2$/rGO/$NiCoO_2$ sandwich sheet is still thin enough, and comparable to that of the pure $NiCoO_2$ sheet. Thus the unique porous architecture of the pure $NiCoO_2$ nanosheets is inherited by the $NiCoO_2$/rGO/$NiCoO_2$ sandwich sheets as shown in Fig. 12(c). The BET specific surface area and pore volume are 138.1 m^2/g and 0.80 cm^3/g for the $NiCoO_2$/rGO/$NiCoO_2$ composite, which are even larger than the pure $NiCoO_2$ (124.8 m^2/g, 0.31 cm^3/g).

CV and galvanostatic charge/discharge measurements were performed on the $NiCoO_2$/rGO/$NiCoO_2$ composite in three electrode configurations to evaluate its electrochemical performance as an electrode of SC. Figure 13(a) shows the typical CV curves of the $NiCoO_2$/rGO/$NiCoO_2$ composite from 5 to 80 mV/s. The shape of the CV curve is distinct from that of electric double-layer capacitance characterized by nearly rectangular CV curves,[61] which

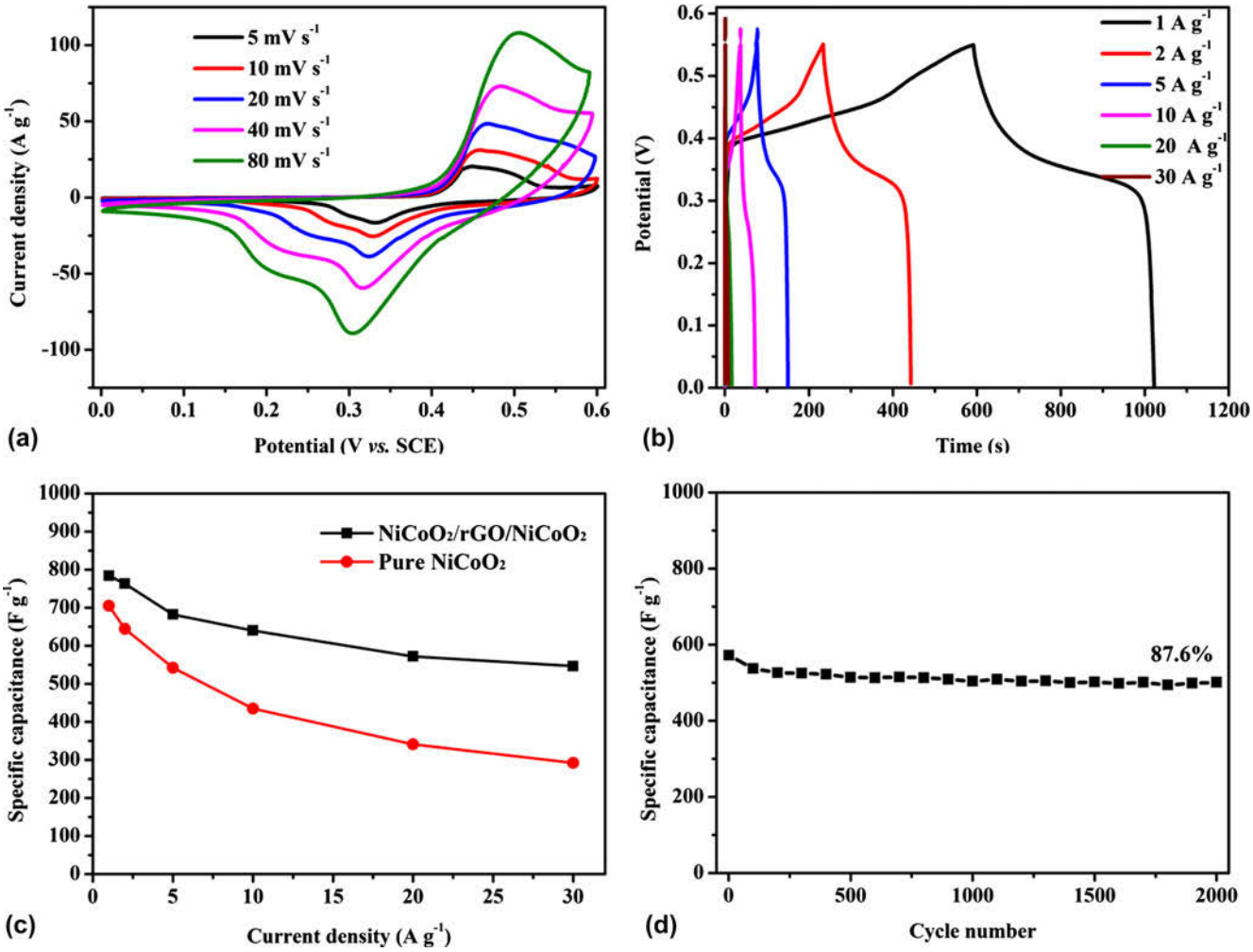

FIG. 13. (a) CV curves and (b) galvanostatic charge/discharge profiles of the $NiCoO_2$/rGO/$NiCoO_2$ electrode in three electrode configurations; (c) specific capacitance of the pure $NiCoO_2$ electrode and $NiCoO_2$/rGO/$NiCoO_2$ electrode at various current densities; (d) cycling performance of the $NiCoO_2$/rGO/$NiCoO_2$ electrode at a current density of 20 A/g.

clearly confirms the pseudocapacitive behavior. Two pairs of well-defined redox peaks can be observed in the CV curves. For the CV curve scanned at the lowest rate of 5 mV/s, two oxidation peaks appear at ~0.44 and 0.48 V in the anodic sweep and two reduction peaks appear at ~0.29 and 0.33 V in the cathodic sweep, which correspond to the Faradaic oxidation/reduction reactions of Ni–O/Ni–O–OH and Co–O/Co–O–OH, respectively. As the scan rate increases, the shape of CV curve is well maintained, indicating that the $NiCoO_2$/rGO/$NiCoO_2$ composite is beneficial for fast redox reactions. But the potential differences between oxidation and reduction peaks also increase with scan rate, which suggests the irreversible reactions and electric polarization.[62] The corresponding charge/discharge curves tested at various current densities are presented in Fig. 13(b). Evidently, there are well-defined voltage plateaus in all these charge/discharge plots, which further suggests the typical pseudocapacitive characteristics. Figure 13(c) shows the relationships between specific capacitance and the current density of pure $NiCoO_2$ and $NiCoO_2$/rGO/$NiCoO_2$. Clearly, the $NiCoO_2$/rGO/$NiCoO_2$ electrode exhibits higher specific capacitance values than pure $NiCoO_2$ electrode at each current density. The $NiCoO_2$/rGO/$NiCoO_2$ electrode gives an excellent pseudocapacitance of 784, 763, 682, 640, 572, and 546 F/g at current density of 1, 2, 5, 10, 20, and 30 A/g, respectively. The higher the current density is loaded, the larger the capacitance gap between the $NiCoO_2$/rGO/$NiCoO_2$ electrode and the pure $NiCoO_2$ electrode is. It suggests that the $NiCoO_2$/rGO/$NiCoO_2$ electrode would benefit from the good conductivity of rGO. The rate performance of the electrode is also good, even compared with recent reported work.[63] The cycling stability, an important indicator for high-efficiency SC, is further evaluated under repeated charge/discharge condition at a constant current density of 20 A/g [Fig. 13(d)]. Impressively, there is only a loss of 12.4% in the specific capacitance even after cycling for 2000 cycles.

The lithium storage performances of the $NiCoO_2$/rGO/$NiCoO_2$ composite were also investigated by assembling them into lithium-ion half-cell batteries. Figure 14(a) displays representative CV profiles of the $NiCoO_2$/rGO/$NiCoO_2$ electrode at a scan rate of 0.2 mV/s between 0.01 and 3 V. Three obvious redox peaks can be clearly identified from every CV curve. For the first cathodic sweep, the dominant cathodic peak locating at around 0.51 V can be attributed to the reduction of Ni^{2+} and Co^{2+} and the formation of SEI film. And the cathodic peak subsequently shifts to around 0.93 V with a reduced intensity in the following scans. In addition, two poorly defined anodic peaks at ~1.45 and 2.23 V could be assigned to the oxidation of metallic Co and Ni to CoO and NiO, respectively. Remarkably, apart from the first cycle, the subsequent cycles overlap well, suggesting the good reversibility of the redox reactions. On the basis of the CV results and previous literature,[64–67] the total electrochemical reaction mechanism could be described by the following electrochemical conversion reaction:

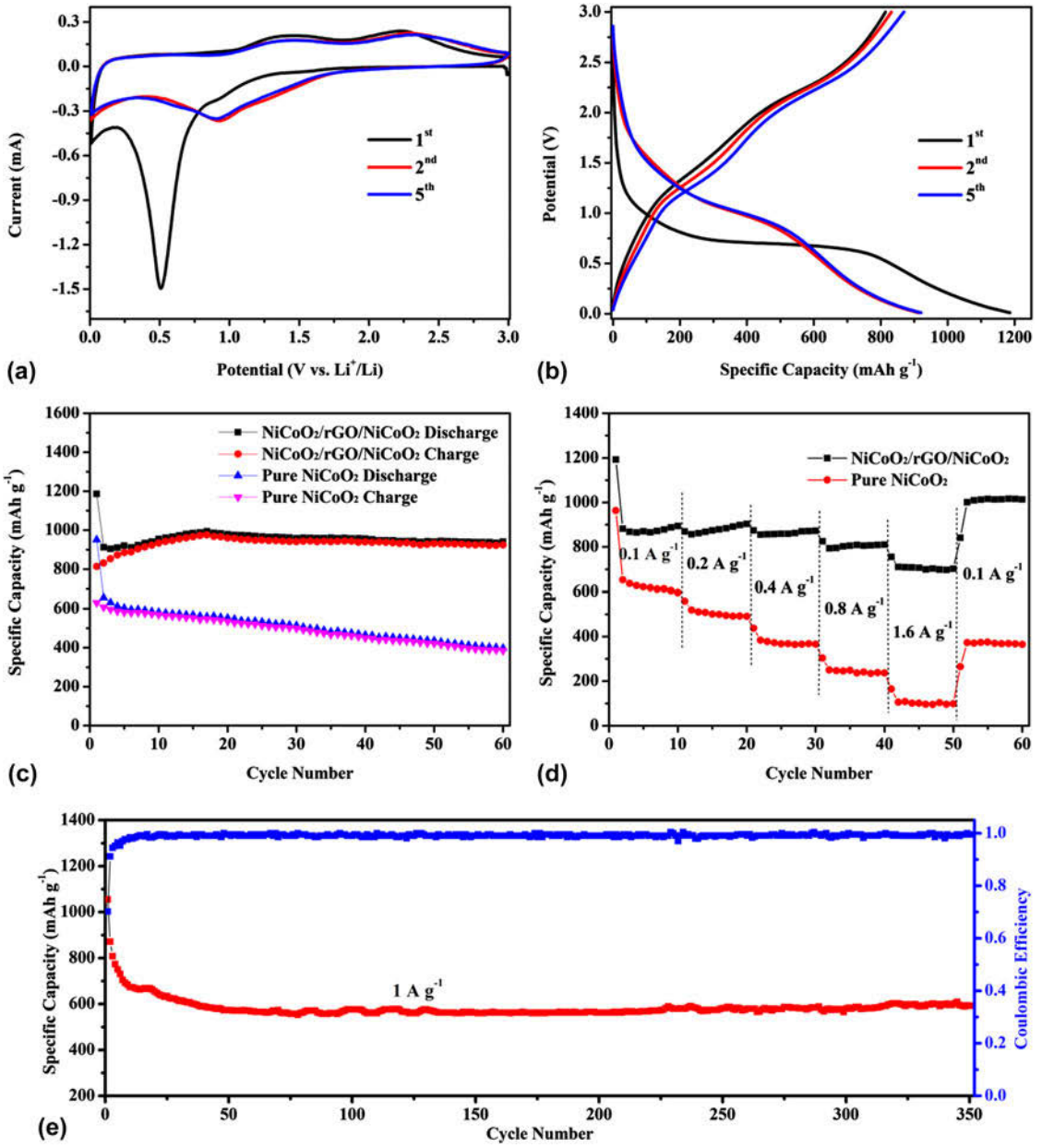

FIG. 14. (a) Representative CV curves at a scan rate of 0.2 mV/s and (b) charge/discharge voltage profiles at a current density of 0.1 A/g of the $NiCoO_2$/rGO/$NiCoO_2$ electrode versus a metallic lithium reference electrode; (c) cycle performances at a current density of 0.1 A/g and (d) rate performances of the pure $NiCoO_2$ and $NiCoO_2$/rGO/$NiCoO_2$ electrode; (e) cycle performance and coulombic efficiency for the $NiCoO_2$/rGO/$NiCoO_2$ electrode at a current density of 1 A/g.

$$NiCoO_2 + 4Li^+ + 4e^- \rightarrow Co + Ni + 2Li_2O \quad . \quad (5)$$

$$Co + Li_2O \leftrightarrow CoO + 2Li^+ + 2e^- \quad . \quad (6)$$

$$Ni + Li_2O \leftrightarrow NiO + 2Li^+ + 2e^- \quad . \quad (7)$$

The typical charge/discharge voltage profiles of $NiCoO_2$/rGO/$NiCoO_2$ composite at a current density of 0.1 A/g are shown in Fig. 14(b). The initial discharge and charge capacities of the electrode are 1186 and 850 mA h/g, respectively, suggesting a coulombic efficiency of 71.7%. The second discharge capacity is 920 mA h/g, suffering 266 mA h/g loss compared to the initial one. That is consistent with the peak intensity decline in the second cathodic sweep of the CV curves. The voltage plateaus of the second discharge curve increases from 0.75 V to 1.1 V, corresponding to the reduction peak shift in the second cathodic curve of the CV curves. The large irreversible capacity loss and the increase of the voltage plateaus should be associated with SEI film formation and electrolyte decomposition.[68,69] The following discharge/charge cycle overlaps the second one very well. The good overlapping of the curves after the first cycle suggests a good electrochemical reversibility. For pure $NiCoO_2$ electrode, the initial discharge and charge capacities are 950 and 633 mA h/g, giving a much lower coulombic efficiency of 66.6%. And it still suffers capacity loss even after the second cycle.

The cyclic performances of the $NiCoO_2$/rGO/$NiCoO_2$ electrode and the pure $NiCoO_2$ electrode are also compared at a current density of 0.1 A/g. As shown in Fig. 14(c), the capacity of pure $NiCoO_2$ continuously drops off during discharge/charge cycle. After 60 cycles, the $NiCoO_2$ electrode only delivers a reversible capacity of 391 mA h/g. For $NiCoO_2$/rGO/$NiCoO_2$ electrode, the reversible capacity is gradually increasing during the initial 17 cycles until it achieves the maximum value of 998 mA h/g, 83.8% of the initial discharge capacity. That capacity can be retained till the 60th cycle. Figure 14(d) show the rate performance of the $NiCoO_2$/rGO/$NiCoO_2$ electrode at different current density (0.1–1.6 A/g). The $NiCoO_2$/rGO/$NiCoO_2$ electrode delivers an average discharge capacity of 880, 886, 856, 807, and 706 mA h/g at current density of 0.1, 0.2, 0.4, 0.8, and 1.6 A/g, respectively. 80.3% of the capacity can be retained even as the current density is enlarged 16 times from 0.1 to 1.6 A/g. Importantly, as the current density returns to 0.1 A/g after the 60 cycles, the electrode releases an even higher reversible capacity (1010 mA h/g) than the initial. In fact, that value is comparable to the one obtained after 60 times cycling of discharge/charge at 0.1 A/g shown in Fig. 14(c). The electrode is so stable that large current density loading does not cause any capacity loss. Its cycle life can be up to 350 cycles at 1 A/g, as shown in Fig. 14(e). The reversible capacity suffers a fast decline in the initial 20 circles and then is maintained at 595 mA h/g for the following 330 cycles. As a contrast, the pure $NiCoO_2$ electrode presents a worse rate capability at each current density and the gap between the reversible capacities of two electrodes expands as the current density increases. The large current density loading also cause unrecoverable capacity loss. As the current density returned to 0.1 A/g, only a half of the initial capacity was retained. The excellent performance of the $NiCoO_2$/rGO/$NiCoO_2$ electrode on storage of lithium is even rare in recent reports of the same kind electrodes.[16,55,64–66,70–75]

EIS measurements were carried out at frequencies from 100 kHz to 0.01 Hz on both as-prepared electrodes. As shown in Fig. 15, the Nyquist plots of the $NiCoO_2$/rGO/$NiCoO_2$ and $NiCoO_2$ electrodes share a similar feature with an inclined line at low frequency region and a depressed semicircle in the high-medium frequency region. The interception on the Z' axis at the high-frequency end denotes the electrolyte resistance (R_e). The size of the semicircle that encompasses the medium-frequency region is a symbol of the charge-transfer resistance (R_{ct}). And the inclined line in the low-frequency response indicates the Warburg impedance related to Li-ion diffusion in the solid.[47,76] Using the equivalent circuit model in the inset of Fig. 15,[39,46] R_{ct} can be obtained by fitting the spectra. It is 52 Ω for the $NiCoO_2$/rGO/$NiCoO_2$ electrode and 92 Ω for the $NiCoO_2$ electrode.

As excellent electrodes of SCs and LIBs, they should be porous, to make sure the access of electrolyte, own high specific surface area and good conductivity.

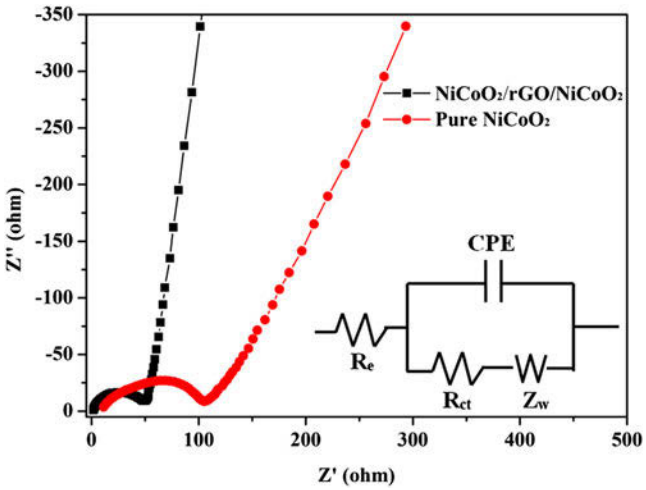

FIG. 15. Nyquist plots of the as-prepared pure $NiCoO_2$ and $NiCoO_2$/rGO/$NiCoO_2$ electrodes versus metallic lithium reference electrodes over the frequency range from 100 kHz to 0.01 Hz at room temperature. And the inset is the fitting equivalent circuit model.

Pseudo-capacitance chemical reaction takes place on the interface of electrode materials with electrolyte. High specific surface area can provide a high ratio of mass on the interface to react and thus guarantee a high specific capacitance. High specific surface area can also supply plenty of reaction sites for LIBs and shorten the route of lithium ion diffusion. Then the LIBs can have large lithium storage and good rate performances. Good conductivity is essential to electrode materials of SCs and LIBs, which can improve the reaction kinetics, power density, output voltage and energy density. The synthesized $NiCoO_2$ sheets in this paper are ultrathin. Although they are crystalline, they can still be randomly wrinkled and needn't keep an invariable contour profile of crystal. As stacking together, the random wrinkled sheets mutually brace each other and build up a unique porous architecture. To improve the conductivity, the rGO sheets with high quality were in situ sandwiched by $NiCoO_2$ sheets in the work, where rGO sheet can act as an expressway for charge transfer. The as-prepared $NiCoO_2$/rGO/$NiCoO_2$ sandwich sheets are as thin as the $NiCoO_2$ sheets. So they can inherit the properties of the $NiCoO_2$ sheets and build up a similar porous architecture like the $NiCoO_2$ sheets. The adding of rGO significantly improves the conductivity of the electrode, as proved by the EIS results in Fig. 15. That makes the electrode have a better rate performance than the pure $NiCoO_2$ electrode in SCs and LIBs. Meanwhile, rGO is ultra-flexible. The large volumetric change of $NiCoO_2$ during lithiation/delithiation can be accommodated by the flexible rGO and the room between the sandwich sheets.[8,56] As the $NiCoO_2$ sheets are firmly anchored with rGO, even if the $NiCoO_2$ sheets pulverized during cycling, they wouldn't peel off from the surface of rGO. Thus, the electrode materials are still active, and the integration of the electrode remains stable. That explains why the cycle life of the SC/LIB using this electrode is pretty long.

IV. ULTRAFINE TMO NANOPARTICLES ENCAPSULATED BY CARBONOUS MATERIALS

Another strategy toward alleviating the poor conductivity and pulverization of TMO is nanostructuring. Compared to the bulk counterparts, nanosized electrode materials own many merits. Firstly, nanosized materials are generally too tiny to be pulverized. Meanwhile the void between the nanosized electrode materials can provide spaces to buffer the mechanical stress induced by the volume change.[18] Consequently, nanostructured electrode materials usually have a higher reversible capacity as well as a longer cycle life than their bulk counterparts. Secondly, nanostructured electrode materials hold a very high surface-to-volume ration, which provide plenty of reaction sites and shorter diffusion paths.[77] Thus, these electrodes present a high rate capacity and a high power density. Substantial efforts have been made on nanostructuring and huge progress has been made on it.[24,50] Meanwhile, these works also obviously show that nanostructuring can't solely solve all the problems thoroughly that transition metal oxides have suffered as LIBs anode materials. Nanoparticles (NPs) tend to aggregate after tens of cycling. This problem has been partially alleviated by separating them by graphene.[11,78–80] But such physical adsorption is not very strong enough. After dozens of circulation, they can also be desorbed from the surface. The nanovoids included in the nanostructured electrode materials can't strongly support the structural stability and integrity. The initial morphology generally loses after dozen of cycles because of pulverization. If these nanovoids can be filled in by some solid materials which not only give a support to the nanostructured materials and buffer the inner stress but also improve the electric conductivity, then the LIBs anode materials are integrated as a unite. The properties of LIBs anode must be meliorated a lot. Thus, Co_3O_4 NPs were successfully synthesized and encapsulated by porous graphitic carbon nanosheets in my lab. It presented very high reversible capacity and excellent cycling stability especially at high rate as LIBs anode.

The overall synthetic procedure of the Co_3O_4@C@PGC nanosheets is schematically illustrated in Fig. 16.[81] Two strategies were involved in this procedure. Firstly, the water-soluble NaCl particle surface was utilized as the template for the nanosheets because NaCl has a face-centered cubic (fcc, $Fm3m$ (225), $a = 0.5642$ nm) crystal structure, and its growth rate can be controlled by varying the concentration and temperature.[48,82,83] Secondly, glucose and cobalt nitrate were chosen as the carbon precursor and the metal precursor, respectively, due to their low cost. In the synthesis, the NaCl, $C_6H_{12}O_6$, and $Co(NO_3)_2$ were first dissolved in distilled water to get a homogeneous solution. After gradually heated to 80 °C, the solution color changed from pink to blue, the sample viscosity increased greatly, and then the polymerization of the glucose began, which resulted in the generation of a very thin frame homogeneously coated on the NaCl particle surface. After that, the composite powders were calcined at 750 °C under N_2. During this process, The Co $(NO_3)_2{\cdot}6H_2O$ was decomposed into oxide. The oxide was subsequently reduced by $C_6H_{12}O_6$ into Co NPs, which is very active to catalyze the decomposition of $C_6H_{12}O_6$ into carbon. The fresh generated carbon usually encapsulated the Co NPs firstly, and then piled up in the form of porous graphitic carbon. As a result, the coating layer on the surface of the NaCl particles was converted to carbon-encapsulated Co NPs embedded in porous graphitic carbon nanosheets (Co@C@PGC nanosheets). In the second step, the Co NPs were further oxidized into Co_3O_4 NPs as the Co@C@PGC nanosheets were calcinated in air. Finally,

the porous graphitic carbon nanosheets in which plenty of Co_3O_4 NPs were embedded (Co_3O_4@C@PGC nanosheets) were obtained on the surface of the NaCl particles.

The morphology of Co@C@PGC and Co_3O_4@C@PGC nanosheets was shown in the SEM image of Figs. 17(a) and 17(b), respectively. As shown in Fig. 17(a), a lot of graphite nanosheets with a thickness of about 20 nm and an area of 1–10 μm^2 interconnected with each other to build up a 3D porous architecture. This architecture can be reserved even after calcinations in air, which is evidenced by the SEM image shown in Fig. 14(b). The inset in Fig. 17(b) clearly shows that the thickness of the

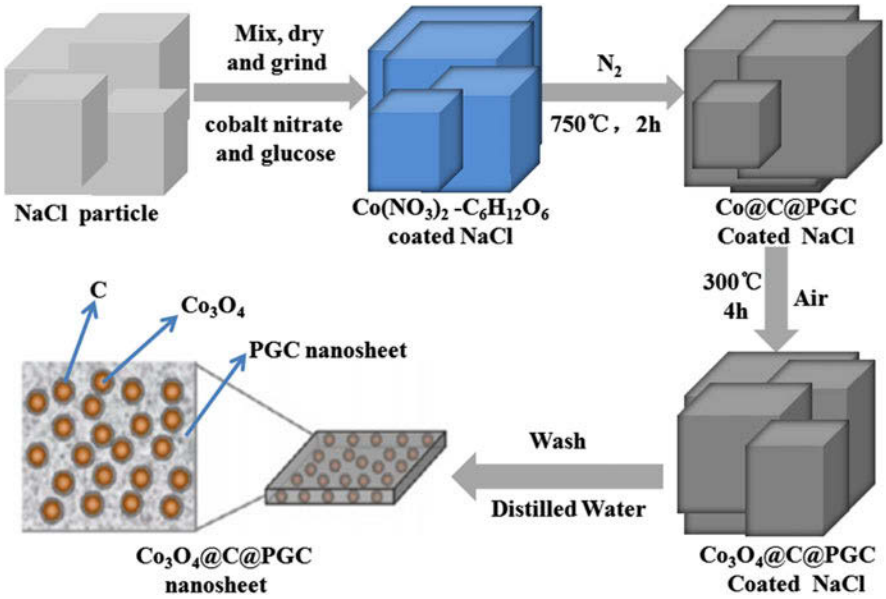

FIG. 16. Schematic illustration of the in situ sol–gel technique to fabricate Co_3O_4@C@PGC nanosheets by using the surface of NaCl particles as the template.

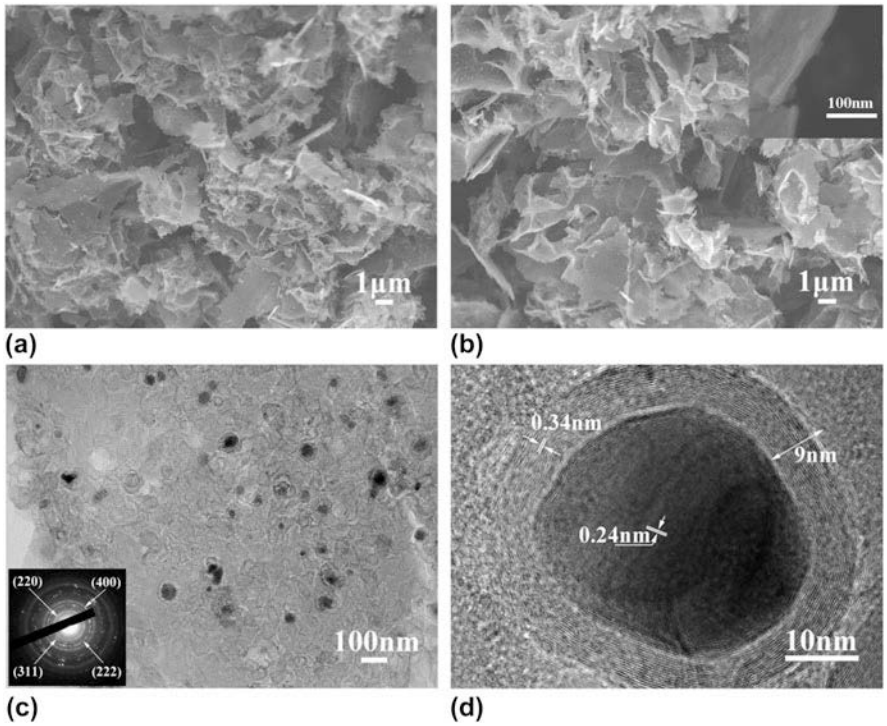

FIG. 17. (a) SEM image of Co@C@PGC nanosheets; (b) SEM image of Co_3O_4@C@PGC nanosheets and the inset is SEM image of high magnification; (c) TEM and (d) HRTEM image of Co_3O_4@C@PGC nanosheets.

nanosheets is around 20 nm. The morphology of Co_3O_4/C composites was also observed by SEM. The flakes are very thicker and larger than Co_3O_4@C@PGC nanosheets. Their thickness is more than 500 nm. There is no interconnection among the flakes. They just pile up on each other, leaving very little space between them. Of course, the space isn't stable, yet. The thin sheets observed in Co@C@PGC and Co_3O_4@C@PGC disappear thoroughly in Co_3O_4/C composites. It suggests that NaCl particles have played a crucial role in building up such 3D porous architecture of nanosheets. A TEM image and HRTEM image of Co_3O_4@C@PGC nanosheets were shown in Figs. 17(a) and 17(d), respectively. The graphite carbon nanosheets seem to be transparent to the electron beam and show a very low contrast in the image, which again suggests that the nanosheet is very thin, around tens of nanometers. The black rings located on the sheet of Fig. 17(c) indicate a foam-like structure of the graphite. Co_3O_4 NPs, with diameters ranging from 5 to 40 nm, are well-dispersed in the PGC nanosheet. The selected area electron diffraction pattern in the inset of Fig. 17(c) further verifies the encapsulated core being Co_3O_4 NPs. In fact, the Co_3O_4 NPs were firmly anchored by the porous graphite nanosheets. As shown in Fig. 17(d), a Co_3O_4 crystal is perfectly encapsulated by thin and well-graphitized onion-like carbon shells. The HRTEM interference fringes of the Co_3O_4 crystal can be clearly discerned. They have a spacing of 0.24 nm, as denoted in Fig. 17(d), which is equal to the spacing of (311) plane of Co_3O_4. The spacing of the interference fringe of the shell is 0.34 nm, which is also equal to the spacing of (002) plane of graphite. And the thickness of graphite shell is about 9 nm. The morphology of Co@C@PGC nanosheets is also characterized by TEM and HRTEM. Carefully comparing the results, it is found that there is little difference on the morphology of the graphite carbon sheets and the crystal sizes. It again makes sure that the calcinations didn't hurt the graphite carbon sheets and none coalescence happened among Co NPs. The Co NPs just was oxidized at its place and converted to Co_3O_4 NPs.

The initial three cycles of the representative cyclic voltammogram (CV) performed on a coin half-cell at room temperature between 0.01 and 3.0 V at a sweep rate of 0.1 mV/s is presented in Fig. 18(a). In accord with previous results, the first cycle shows lots of differences from the subsequent ones on CV curves, especially on the discharge branch.[29,50,84] In the first discharge process, the obvious cathodic peak was located at around 0.97 V, which was attributed to the electrochemical reduction of Co_3O_4 to metallic cobalt accompanying the formation of Li_2O and the solid electrolyte interphase (SEI) film.[84–86] In the anodic process, broad peaks located at around 2.15 V can be ascribed to the reversible oxidation reaction from cobalt to Co_3O_4.[78] The total electrochemical reaction mechanism of Co_3O_4 anode can be described by the following electrochemical conversion reaction[87]:

$$Co_3O_4 + 8Li \leftrightarrow 4Li_2O + 3Co \quad .$$

The main reduction peak is shifted to ~1.15 V, and the peak intensity drops significantly from the second cycle, indicating the occurrence of some irreversible reactions associated with formation of the SEI film in the first cycle.[88] On the other hand, the oxidation peak at ~2.2 V in the anodic sweep exhibits little change during the three cycles, suggesting that the SEI formed on the PGC nanosheets surfaces in the first cycle is very stable.

Typical galvanostatic charge/discharge curves of the Co_3O_4@C@PGC nanosheets electrodes at a current density of 0.1 A/g between 0.01 and 3.00 V are shown in Fig. 18(b). The initial charge and discharge capacities are approximately 1187 and 1859 mA h/g, respectively, resulting in an initial coulombic efficiency of ~64%. The initial irreversible capacity loss of the Co_3O_4@C@PGC nanosheets could be associated with the inevitable formation of SEI and decomposition of electrolyte[8,9,85,89] and in good agreement with the above CV results. The discharge voltage plateau at ~1.1 V in the first cycle shift to ~1.2 V since the second cycle, just corresponding to the shift of reduce peak in CV curves from 0.97 V to 1.15 V. The areas under the charge and discharge curves are comparable, indicating a very low energy loss during charge/discharge. Starting from the 10th cycle, both charge and discharge curves are overlapping the previous one up to the 100th cycle, which indicates that the Co_3O_4@C@PGC nanosheets exhibit excellent cycle stability.[79,90]

The cycle performances of the Co_3O_4@C@PGC nanosheets, Co_3O_4/C composite and Co_3O_4 NPs were investigated at a current density of 0.1 A/g. The results were shown in Fig. 18(c). The Co_3O_4@C@PGC nanosheets electrode has the best cyclic retention and the highest reversible capacity. After 100 cycles, the reversible capacity is as high as 1413 mA h/g. The capacity is even higher than the theoretical capacity of Co_3O_4. Such high specific capacity should be attributed to the following points: firstly, the PGC nanosheets have a reversible capacity of 580 mA h/g, and there would be synergetic effects between PGC nanosheets and Co_3O_4 NPs,[85] which can also contribute to the lithium storage capacity. Secondly, the reversible decomposition of the electrolyte with the formation of SEI and extra lithium ion adsorption/desorption on the SEI during cycling may lead to the high experimental lithium storage capacity as well.[41,91] In contrast, the reversible capacity of the Co_3O_4/C composite is much lower, which is only ~763 mA h/g at the end of the 100 cycles. But it also has an excellent cycling performance. Although, the bulk carbon in Co_3O_4/C composite prevents the Co_3O_4 NPs from playing their best in the lithium storage capacity, it

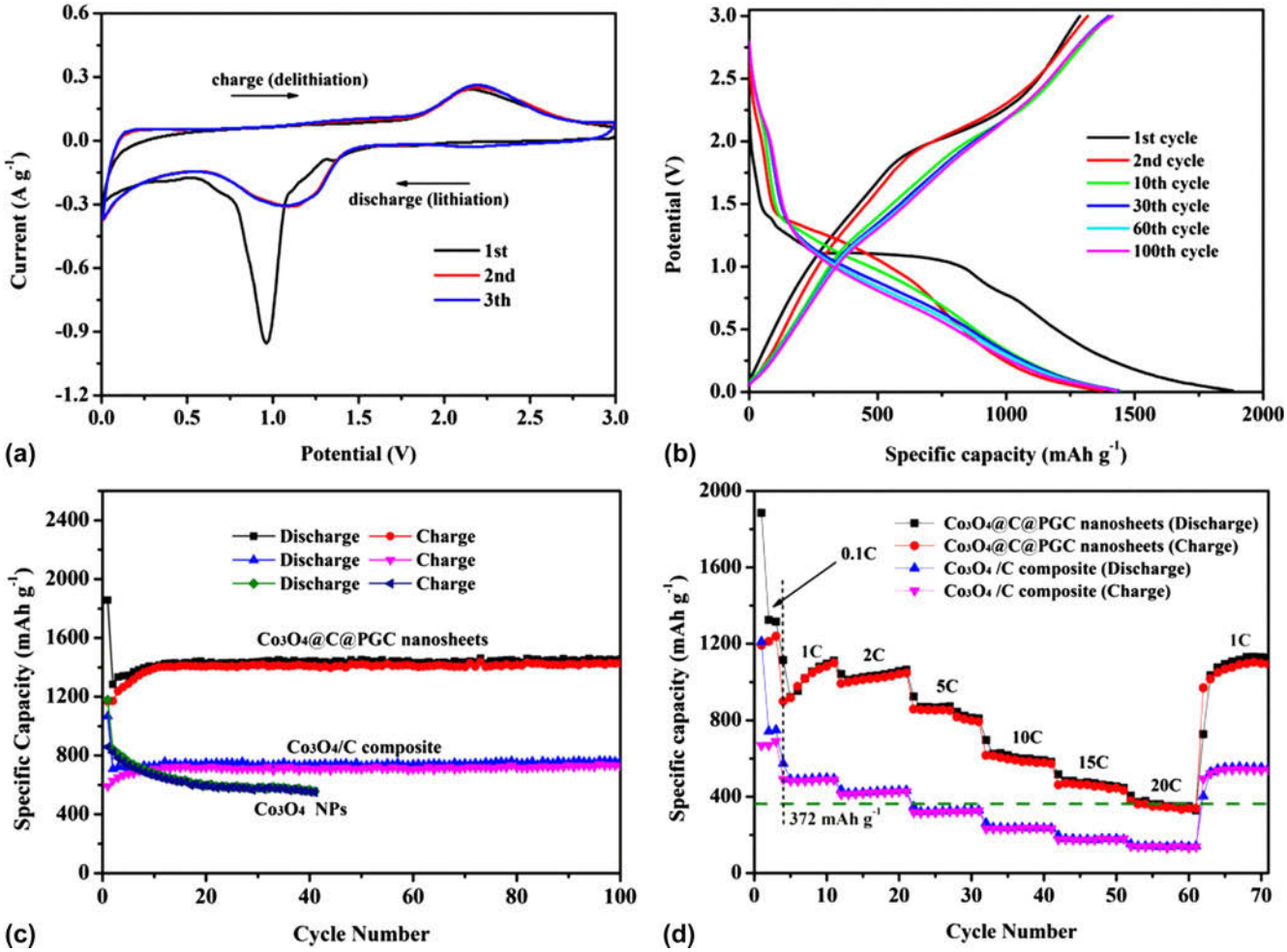

FIG. 18. (a) Representative CV curves of an electrode based on the Co_3O_4@C@PGC nanosheets obtained at a voltage range of 0.0–3.0 V (vs Li^+/Li) and potential scan rate of 0.1 mV/s. (b) Voltage profiles of the Co_3O_4@C@PGC nanosheets electrode at a current density of 0.1C. (c) Charge/discharge capacities of the Co_3O_4@C@PGC nanosheets, Co_3O_4/C composite and Co_3O_4 NPs at a current density of 0.1C. (d) Rate capabilities and cycle performance of Co_3O_4@C@PGC nanosheets and Co_3O_4/C composite electrodes cycled at different rates from 0.1 to 20C (1C = 1 A/g).

still takes an important role in holding the integrality of the structure. The Co_3O_4 NPs show the fastest capacity fading and the lowest reversible capacity which is below 549 mA h/g after 40 cycles. In the case of bare Co_3O_4 NPs, SEI trends toward rupture to accommodate the volume change induced by Li^+ expansion/contraction. The Co NPs forming in discharging processes also have catalyzing effect on SEI and are harmful to the integrality of the film. Thus the electrode material surface will cyclically expose itself to the electrolyte and more and more SEI films consecutively form on it, which leads to continual consuming of electrolyte and the fast capacity fading.[5,92] However, a very thin carbon shell covers the electrode material in Co_3O_4@C@PGC nanosheets, which induces a strong synergistic effect between porous graphitic carbon nanosheets and carbon-encapsulated Co_3O_4 NPs.[92] During the charge/discharge process, the carbon shell is very beneficial to stabilize SEI film and avoid rupturing. Meanwhile, it is also effective to prevent the Co_3O_4 NPs from agglomerating. The porous sheet structure of carbon which links the shelled Co_3O_4 NPs provides enough space to accommodate the huge volume changes. In addition, the high specific surface area of Co_3O_4@C@PGC nanosheets ensures a high contact area between the electrode and electrolyte. So Li^+ has plentiful diffusion accesses from electrolyte into electrode interior, which will intensively enhance the transport rate of Li^+. All these factors are vital for the electrode to retain the excellent cycling stability and high reversible storage capability.[16]

The electrode made by Co_3O_4@C@PGC nanosheets also has the best rate capability, as shown in Fig. 18(d). After three cycles at 0.1C, the electrodes were firstly tested at 1C (1C = 1 A/g). It is obvious that the Co_3O_4@C@PGC electrode still needs ten more cycles to activate all active materials for its reversible capacity

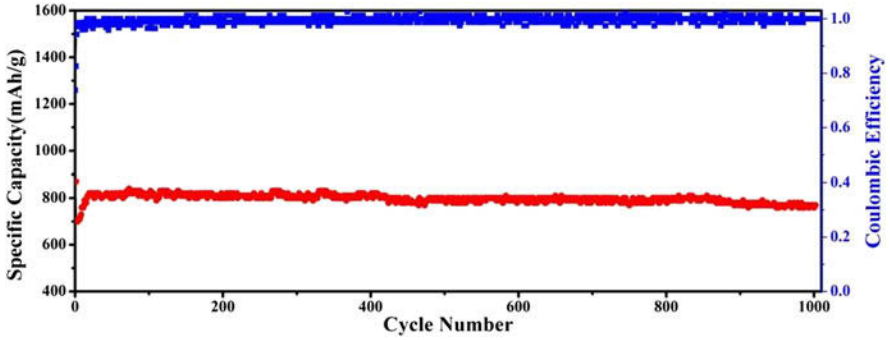

FIG. 19. Cycle performance and coulombic efficiency for the Co_3O_4@C@PGC nanosheets electrode at higher current density of 5C.

increases with cycle number until the 11th cycle.[27,87] Meanwhile, the Co_3O_4@C composite electrode shows a stable capacity as tested at 1C. The reversible capacity of the Co_3O_4@C@PGC nanosheets electrode reaches a very high value of 1105 mA h/g at the 11th cycle,[78,93] while the Co_3O_4@C composite electrode maintains a reversible capacity of 502 mA h/g during these cycles. At each tested specific current density including 2, 5, 10, and 15C, the average reversible capacity of the Co_3O_4@C@PGC electrode (1030, 845, 560, and 461 mA h/g) is much higher than Co_3O_4@C composite electrode (430, 323, 240, 185 mA h/g). At most of specific current density except of 20C, the reversible capacity of the Co_3O_4@C@PGC electrode is larger than the theoretical capacity of a commercial graphite anode (~372 mA h/g).[89] Even at 20C, the average reversible capacity (345 mA h/g) is still very close to the theoretical capacity of graphite. When the current rate finally returns to the initial value of 1C after 61 cycles, the electrode can recover its initial capacity of 1030 mA h/g with a little bit loss. And it is still sustainable up to the 70th cycle.

To further confirm the durability of this nanosheet anode to work at higher rate, the cyclability of the Co_3O_4@C@PGC nanosheets electrode has been further investigated upon 1000 cycles at 5C and the result is shown in Fig. 19. In the initial 20 cycles, the specific capacity gradually increases up to 820 mA h/g, corresponding to a process of activating the active substance, which is common in the literature.[27,87] It is striking to note that the specific capacity can remain as high as 760 mA h/g even after 1000 cycles. Firstly, the well-graphitized carbon shells firmly cover Co_3O_4 NPs and integrate into PGC nanosheets. Thus, a continuous network is constructed by the conductive carbon, which ensures the electron transport freely. The porous structure of the nanosheets provides a huge interfacial area with electrolyte. The electrode has abundant accesses for Li^+ to interior active materials. The thin film structure of Co_3O_4@C@PGC nanosheets shortens the diffusion path of Li^+. So the electrode can work very well at a very high specific current density. Meanwhile, the thin carbon shells separate Co_3O_4 NPs from electrolyte and each other. So a firm and stable SEI film can form on the carbon surface because the side reaction between SEI film and Co_3O_4 NPs is effectively blocked. And the aggregation Co_3O_4 NPs can also be suppressed. Carbon materials always have good mechanical flexibility, which endow the shells with the ability to expand and contract with Co_3O_4 NPs during lithium ion insertion/extraction process. Finally, the volume change is accommodated by the abundant macropore and mesopore in the PGC nanosheets. Thus, the electrode shows a good cycling stability. At last, the thin film structure is also very favorable for the adsorption of lithium ions on both sides, edges, and other defects of these nanosheets.[92,94] That endows the electrode with an ultrahigh lithium storage capability.

V. CONCLUSION

No method can really prevent TMO from pulverization, because it is related to the Li ion storage mechanism. During discharge process, the TMO is reduced into metal nanoparticles which homogeneously distributes in a Li_2O matrix. During charge process, the Li_2O matrix disappears and the metal nanoparticles have little change to unite into a bulk metal oxide. Provided the nanoparticles keep activation, pulverization is not harmful, or even good for the reversible capacity, because the nanoparticles generated from pulverization can shorten the Li ion diffusion and electron transfer distance. How to keep the nanoparticles active is the key point to saving the capacity fading of TMO anodes. In our lab, we have tried SEI film and rGO to improve the stability of the structure. That purpose has been achieved to some extent. But the product is still far from commercial. It seems that those strategies just can alleviate but can't stop the fading of the capacity. Pulverization also has a limitation, beyond which pulverization can't happen. Thus we synthesized ultrafine nanoparticle of cobaltosic oxide, the diameter of which is close

to 10 nm. Then the nanoparticles were encapsulated by porous graphitic carbon. The nanoparticles can still pulverize during lithium ion insertion/extraction process, but they would be split into finite particles. All the particles can be encapsulated by and connected with the well-graphitized carbon shells. So they still can react with lithium ion and keep active. The electrode made by this method has a very stable reversible capacity until 1000 cycles. The large over voltage problem of TMO anode is related to the kinetic transport at the electrode/electrolyte interface and in the inner TMO. Nanoparticles generated from pulverization can also generate more reaction site and shorten the Li ion diffusion path. Thus, the rate performance of the electrode is also excellent. 30% capacity of the electrode can be charged/discharged in 3 min.

ACKNOWLEDGMENTS

This work was supported by National Natural Science Foundation of China (Grant No. 51401083, 51371089, 51601067, 51475200 and 51631004), and Program for Innovative Research Team (in Science and Technology) in University of Jilin Province, and Technology Development Project of Jilin Province (No. 20150519007JH).

REFERENCES

1. B. Zhao, R. Ran, M. Liu, and Z. Shao: A comprehensive review of $Li_4Ti_5O_{12}$-based electrodes for lithium-ion batteries: The latest advancements and future perspectives. *Mater. Sci. Eng., R* **98**, 1 (2015).
2. H-G. Jung, S-T. Myung, C.S. Yoon, S-B. Son, K.H. Oh, K. Amine, B. Scrosati, and Y-K. Sun: Microscale spherical carbon-coated $Li_4Ti_5O_{12}$ as ultra high power anode material for lithium batteries. *Energy Environ. Sci.* **4**(4), 1345 (2011).
3. P.G. Bruce, B. Scrosati, and J.M. Tarascon: Nanomaterials for rechargeable lithium batteries. *Angew. Chem.* **47**(16), 2930 (2008).
4. B. Dunn, H. Kamath, and J-M. Tarascon: Electrical Energy Storage for the Grid A Battery of Choices. *Science* **334**(6058), 928 (2011).
5. H. Kim, D-H. Seo, S-W. Kim, J. Kim, and K. Kang: Highly reversible Co_3O_4/graphene hybrid anode for lithium rechargeable batteries. *Carbon* **49**(1), 326 (2011).
6. M. Armand and J-M. Tarascon: Building better batteries. *Nature* **451**, 652 (2008).
7. L. Ji, Z. Lin, M. Alcoutlabi, and X. Zhang: Recent developments in nanostructured anode materials for rechargeable lithium-ion batteries. *Energy Environ. Sci.* **4**(8), 2682 (2011).
8. Y. Chen, M. Zhuo, J. Deng, Z. Xu, Q. Li, and T. Wang: Reduced graphene oxide networks as an effective buffer matrix to improve the electrode performance of porous $NiCo_2O_4$ nanoplates for lithium-ion batteries. *J. Mater. Chem. A* **2**(12), 4449 (2014).
9. G. Gao, H.B. Wu, and X.W.D. Lou: Citrate-Assisted Growth of $NiCo_2O_4$ Nanosheets on Reduced Graphene Oxide for Highly Reversible Lithium Storage. *Adv. Energy Mater.* **4**, 1400422 (2014).
10. J. Guo, L. Chen, X. Zhang, B. Jiang, and L. Ma: Sol-gel synthesis of mesoporous Co_3O_4 octahedra toward high-performance anodes for lithium-ion batteries. *Electrochim. Acta* **129**, 410 (2014).
11. X-L. Huang, R-Z. Wang, D. Xu, Z-L. Wang, H-G. Wang, J-J. Xu, Z. Wu, Q-C. Liu, Y. Zhang, and X-B. Zhang: Homogeneous CoO on Graphene for Binder-Free and Ultralong-Life Lithium Ion Batteries. *Adv. Funct. Mater.* **23**(35), 4345 (2013).
12. Y. Huang, X-L. Huang, J-S. Lian, D. Xu, L-M. Wang, and X-B. Zhang: Self-assembly of ultrathin porous NiO nanosheets/graphene hierarchical structure for high-capacity and high-rate lithium storage. *J. Mater. Chem.* **22**(7), 2844 (2012).
13. E. Kang, Y.S. Jung, A.S. Cavanagh, G-H. Kim, S.M. George, A.C. Dillon, J.K. Kim, and J. Lee: Fe_3O_4 Nanoparticles Confined in Mesocellular Carbon Foam for High Performance Anode Materials for Lithium-Ion Batteries. *Adv. Funct. Mater.* **21**(13), 2430 (2011).
14. A. Li, H. Song, W. Wan, J. Zhou, and X. Chen: Copper oxide nanowire arrays synthesized by in-situ thermal oxidation as an anode material for lithium-ion batteries. *Electrochim. Acta* **132**, 42 (2014).
15. J. Song, J. Duay, E. Gillette, and S.B. Lee: The reversible anomalous high lithium capacity of MnO_2 nanowires. *Chem. Commun.* **50**(55), 7352 (2014).
16. M. Zhang, F. Yan, X. Tang, Q. Li, T. Wang, and G. Cao: Flexible CoO–graphene–carbon nanofiber mats as binder-free anodes for lithium-ion batteries with superior rate capacity and cyclic stability. *J. Mater. Chem. A* **2**(16), 5890 (2014).
17. J. Liu, Y. Xu, X. Ma, J. Feng, Y. Qian, and S. Xiong: Multifunctional CoO@C metasequoia arrays for enhanced lithium storage. *Nano Energy* **7**, 52 (2014).
18. P. Poizot, S. Laruelle, S. Grugeon, L. Dupont, and J.M. Tarascon: Nano-sized transition-metal oxides as negative-electrode materials for lithium-ion batteries. *Nature* **407**(6803), 496 (2000).
19. J. Ma, J. Wang, Y-S. He, X-Z. Liao, J. Chen, J-Z. Wang, T. Yuan, and Z-F. Ma: A solvothermal strategy: one-step in situ synthesis of self-assembled 3D graphene-based composites with enhanced lithium storage capacity. *J. Mater. Chem. A* **2**(24), 9200 (2014).
20. M. Winter: The solid electrolyte interphase—The most important and the least understood solid electrolyte in rechargeable Li batteries. *Z. Phys. Chem.*, 1395 (2009).
21. H. Wu, G. Chan, J.W. Choi, I. Ryu, Y. Yao, M.T. Mcdowell, S.W. Lee, A. Jackson, Y. Yang, L. Hu, and Y. Cui: Stable cycling of double-walled silicon nanotube battery anodes through solid-electrolyte interphase control. *Nat. Nanotechnol.* **7**(5), 310 (2012).
22. P. Verma, P. Maire, and P. Novák: A review of the features and analyses of the solid electrolyte interphase in Li-ion batteries. *Electrochim. Acta* **55**(22), 6332 (2010).
23. X. Leng, Y. Shao, S. Wei, Z. Jiang, J. Lian, G. Wang, and Q. Jiang: Ultrathin Mesoporous $NiCo_2O_4$ Nanosheet Networks as High-Performance Anodes for Lithium Storage. *ChemPlusChem* **80**, 1725 (2015).
24. X. Wang, L. Qiao, X. Sun, X. Li, D. Hu, Q. Zhang, and D. He: Mesoporous NiO nanosheet networks as high performance anodes for Li ion batteries. *J. Mater. Chem. A* **1**(13), 4173 (2013).
25. B. Qu, L. Hu, Q. Li, Y. Wang, L. Chen, and T. Wang: High-performance lithium-ion battery anode by direct growth of hierarchical $ZnCo_2O_4$ nanostructures on current collectors. *ACS Appl. Mater. Interfaces* **6**(1), 731 (2014).
26. Y. Chen, J. Zhu, B. Qu, B. Lu, and Z. Xu: Graphene improving lithium-ion battery performance by construction of $NiCo_2O_4$/graphene hybrid nanosheet arrays. *Nano Energy* **3**, 88 (2014).
27. C. Peng, B. Chen, Y. Qin, S. Yang, C. Li, Y. Zuo, S. Liu, and J. Yang: Facile Ultrasonic Synthesis of CoO Quantum Dot_Graphene Nanosheet Composites with High Lithium Storage Capacity. *ACS Nano* **6**, 1074 (2012).

28. X. Li, X. Zang, Z. Li, X. Li, P. Li, P. Sun, X. Lee, R. Zhang, Z. Huang, K. Wang, D. Wu, F. Kang, and H. Zhu: Large-Area Flexible Core-Shell Graphene/Porous Carbon Woven Fabric Films for Fiber Supercapacitor Electrodes. *Adv. Funct. Mater.* **23**(38), 4862 (2013).
29. B. Luo, B. Wang, M. Liang, J. Ning, X. Li, and L. Zhi: Reduced graphene oxide-mediated growth of uniform tin-core/carbon-sheath coaxial nanocables with enhanced lithium ion storage properties. *Adv. Mater.* **24**(11), 1405 (2012).
30. Y. Fang, Y. Lv, R. Che, H. Wu, X. Zhang, D. Gu, G. Zheng, and D. Zhao: Two-dimensional mesoporous carbon nanosheets and their derived graphene nanosheets: synthesis and efficient lithium ion storage. *J. Am. Chem. Soc.* **135**(4), 1524 (2013).
31. B.P.N. Nguyen, N.A. Kumar, J. Gaubicher, F. Duclairoir, T. Brousse, O. Crosnier, L. Dubois, G. Bidan, D. Guyomard, and B. Lestriez: Nanosilicon-Based Thick Negative Composite Electrodes for Lithium Batteries with Graphene as Conductive. *Adv. Energy Mater.* **3**(10), 1351 (2013).
32. S-M. Paek, E. Yoo, and I. Honma: Enhanced Cyclic Performance and Lithium Storage Capacity of SnO_2/Graphene Nanoporous Electrodes with Three-Dimensionally Delaminated Flexible Structure. *Nano Lett.* **9**(1), 72 (2009).
33. C. Gu, H. Zhang, X. Wang, and J. Tu: One-pot synthesis of SnO_2/reduced graphene oxide nanocomposite in ionic liquid-based solution and its application for lithium ion batteries. *Mater. Res. Bull.* **48**(10), 4112 (2013).
34. C.D. Gu, Y.J. Mai, J.P. Zhou, and J.P. Tu: SnO_2 nanocrystallite: novel synthetic route from deep eutectic solvent and lithium storage performance. *Funct. Mater. Lett.* **04**(04), 377 (2011).
35. L. Zhang, L. Zhao, and J. Lian: Nanostructured Mn_3O_4–reduced graphene oxide hybrid and its applications for efficient catalytic decomposition of Orange II and high lithium storage capacity. *RSC Adv.* **4**(79), 41838 (2014).
36. X. Zhang, J. Zhou, H. Song, X. Chen, Y.V. Fedoseeva, A.V. Okotrub, and L.G. Bulusheva: "Butterfly Effect" In CuO/Graphene Composite Nanosheets: A Small Interfacial Adjustment Triggers Big Changes in Electronic Structure and Li-Ion Storage Performance. *ACS Appl. Mater. Interfaces* **6**(19), 17236 (2014).
37. X. Zhu, X. Song, X. Ma, and G. Ning: Enhanced electrode performance of Fe_2O_3 nanoparticle-decorated nanomesh graphene as anodes for lithium-ion batteries. *ACS Appl. Mater. Interfaces* **6**(10), 7189 (2014).
38. G. Zhou, D-W. Wang, L-C. Yin, N. Li, F. Li, and H-M. Cheng: Oxygen Bridges between NiO Nanosheets and Graphene for Improvement of Lithium Storage. *ACS Nano.* **6**(4), 3214 (2012).
39. X. Leng, X. Ding, J. Hu, S. Wei, Z. Jiang, J. Lian, G. Wang, Q. Jiang, and J. Liu: In situ prepared reduced graphene oxide/CoO nanowires mutually-supporting porous structure with enhanced lithium storage performance. *Electrochim. Acta* **190**, 276 (2016).
40. X. Leng, Y. Shao, S. Wei, Z. Jiang, J. Lian, G. Wang, and Q. Jiang: Ultrathin Mesoporous $NiCo_2O_4$ Nanosheet Networks as High-Performance Anodes for Lithium Storage. *Chempluschem* **80**(12), 1725 (2015).
41. K.T. Nam, D.W. Kim, P.J. Yoo, C.Y. Chiang, N. Meethong, P.T. Hammond, Y.M. Chiang, and A.M. Belcher: Virus-enabled synthesis and assembly of nanowires for lithium ion battery electrodes. *Science* **312**(5775), 885 (2006).
42. X. Song, Q. Ru, Y. Mo, L. Guo, S. Hu, and B. An: A novel porous coral-like $Zn_{0.5}Ni_{0.5}Co_2O_4$ as an anode material for lithium ion batteries with excellent rate performance. *J. Power Sources* **269**, 795 (2014).
43. W. Xu, K. Zhao, C. Niu, L. Zhang, Z. Cai, C. Han, L. He, T. Shen, M. Yan, L. Qu, and L. Mai: Heterogeneous branched core–shell SnO_2–PANI nanorod arrays with mechanical integrity and three dimentional electron transport for lithium batteries. *Nano Energy* **8**, 196 (2014).
44. K.E. Aifantis, T. Huang, S.A. Hackney, T. Sarakonsri, and A. Yu: Capacity fade in Sn-C nanopowder anodes due to fracture. *J. Power Sources* **197**(2), 246 (2012).
45. M.M. Rahman, J-Z. Wang, M.F. Hassan, D. Wexler, and H.K. Liu: Amorphous Carbon Coated High Grain Boundary Density Dual Phase $Li_4Ti_5O_{12}$-TiO_2: A Nanocomposite Anode Material for Li-Ion Batteries. *Adv. Energy Mater.* **1**(2), 212 (2011).
46. Y. Luo, J. Luo, J. Jiang, W. Zhou, H. Yang, X. Qi, H. Zhang, H.J. Fan, D.Y.W. Yu, C.M. Li, and T. Yu: Seed-assisted synthesis of highly ordered TiO_2@α-Fe_2O_3 core/shell arrays on carbon textiles for lithium-ion battery applications. *Energy Environ. Sci.* **5**(4), 6559 (2012).
47. Q. Zhang, C. Zhang, B. Li, S. Kang, X. Li, and Y. Wang: Preparation and electrochemical properties of Ca-doped $Li_4Ti_5O_{12}$ as anode materials in lithium-ion battery. *Electrochim. Acta* **98**, 146 (2013).
48. J. Qin, C. He, N. Zhao, Z. Wang, C. Shi, E-Z. Liu, and J. Li: Graphene Networks Anchored with Sn@Graphene as Lithium Ion Battery Anode. *ACS Nano* **8**, 1728 (2014).
49. L. Hu, H. Zhong, X. Zheng, Y. Huang, P. Zhang, and Q. Chen: $CoMn_2O_4$ spinel hierarchical microspheres assembled with porous nanosheets as stable anodes for lithium-ion batteries. *Sci. Rep.* **2**, 986 (2012).
50. L. Li, Y. Cheah, Y. Ko, P. Teh, G. Wee, C. Wong, S. Peng, and M. Srinivasan: The facile synthesis of hierarchical porous flower-like $NiCo_2O_4$ with superior lithium storage properties. *J. Mater. Chem. A* **1**(36), 10935 (2013).
51. A.K. Mondal, D. Su, S. Chen, X. Xie, and G. Wang: Highly porous $NiCo_2O_4$ Nanoflakes and nanobelts as anode materials for lithium-ion batteries with excellent rate capability. *ACS Appl. Mater. Interfaces* **6**(17), 14827 (2014).
52. M. Li, X. Li, W. Li, X. Meng, Y. Yu, and X. Sun: Atomic layer deposition derived amorphous TiO_2 thin film decorating graphene nanosheets with superior rate capability. *Electrochem. Commun.* **57**, 43 (2015).
53. Y. Zhao, X. Li, B. Yan, D. Li, S. Lawes, and X. Sun: Significant impact of 2D graphene nanosheets on large volume change tin-based anodes in lithium-ion batteries: A review. *J. Power Sources* **274**, 869 (2015).
54. X. Li, X. Meng, J. Liu, D. Geng, Y. Zhang, M.N. Banis, Y. Li, J. Yang, R. Li, X. Sun, M. Cai, and M.W. Verbrugge: Tin Oxide with Controlled Morphology and Crystallinity by Atomic Layer Deposition onto Graphene Nanosheets for Enhanced Lithium Storage. *Adv. Funct. Mater.* **22**(8), 1647 (2012).
55. Y. Sun, X. Hu, W. Luo, and Y. Huang: Ultrathin CoO/Graphene Hybrid Nanosheets: A Highly Stable Anode Material for Lithium-Ion Batteries. *J. Phys. Chem. C* **116**(39), 20794 (2012).
56. G. Gao, H.B. Wu, and X.W.D. Lou: Citrate-Assisted Growth of $NiCo_2O_4$ Nanosheets on Reduced Graphene Oxide for Highly Reversible Lithium Storage. *Adv. Energy Mater.* **4**, 1400422 (2014).
57. J. Li, S. Xiong, Y. Liu, Z. Ju, and Y. Qian: High electrochemical performance of monodisperse NiCo(2)O(2) mesoporous microspheres as an anode material for Li-ion batteries. *ACS Appl. Mater. Interfaces* **5**(3), 981 (2013).
58. X. Leng, Y. Shao, L. Wu, S. Wei, Z. Jiang, G. Wang, Q. Jiang, and J. Lian: A unique porous architecture built by ultrathin wrinkled $NiCoO_2$/rGO/$NiCoO_2$ sandwich nanosheets for pseudocapacitance and Li ion storage *J. Mater. Chem. A* **4**(26), 10304 (2016).
59. S.Q. Chen and Y. Wang: Microwave-assisted synthesis of a Co_3O_4–graphene sheet-on-sheet nanocomposite as a superior anode material for Li-ion batteries. *J. Mater. Chem.* **20**(43), 9735 (2010).

60. J. Liang, R. Ma, N. Iyi, Y. Ebina, K. Takada, and T. Sasaki: Topochemical Synthesis, Anion Exchange, and Exfoliation of Co–Ni Layered Double Hydroxides: A Route to Positively Charged Co–Ni Hydroxide Nanosheets with Tunable Composition. *Chem. Mater.* **22**(2), 371 (2010).
61. X. Cui, R. Lv, R.U.R. Sagar, C. Liu, and Z. Zhang: Reduced graphene oxide/carbon nanotube hybrid film as high performance negative electrode for supercapacitor. *Electrochim. Acta* **169**, 342 (2015).
62. Y. Feng, H. Zhang, Y. Zhang, Y. Bai, and Y. Wang: Novel peapod NiO nanoparticles encapsulated in carbon fibers for high-efficiency supercapacitors and lithium-ion batteries. *J. Mater. Chem. A* **4**(9), 3267 (2016).
63. Y. Xu, J. Wei, L. Tan, J. Yu, and Y. Chen: A Facile approach to $NiCoO_2$ intimately standing on nitrogen doped graphene sheets by one-step hydrothermal synthesis for supercapacitors. *J. Mater. Chem. A* **3**(13), 7121 (2015).
64. X. Xu, B. Dong, S. Ding, C. Xiao, and D. Yu: Hierarchical $NiCoO_2$ nanosheets supported on amorphous carbon nanotubes for high-capacity lithium-ion batteries with a long cycle life. *J. Mater. Chem. A* **2**(32), 13069 (2014).
65. K. Xie, P. Wu, Y. Zhou, Y. Ye, H. Wang, Y. Tang, Y. Zhou, and T. Lu: Nitrogen-doped carbon-wrapped porous single-crystalline CoO nanocubes for high-performance lithium storage. *ACS Appl. Mater. Interfaces* **6**(13), 10602 (2014).
66. Y. Liu, Y. Zhao, Y. Yu, M. Ahmad, and H. Sun: Facile synthesis of single-crystal mesoporous $CoNiO_2$ nanosheets assembled flowers as anode materials for lithium-ion batteries. *Electrochim. Acta* **132**, 404 (2014).
67. X. Ge, C.D. Gu, X.L. Wang, and J.P. Tu: Anomalous self-reduction of layered double hydroxide (LDH): from α-$Ni(OH)_2$ to hexagonal close packing (HCP) Ni/NiO by annealing without a reductant. *Chem. Commun.* **51**(6), 1004 (2015).
68. H. Guan, X. Wang, H. Li, C. Zhi, T. Zhai, Y. Bando, and D. Golberg: CoO octahedral nanocages for high-performance lithium ion batteries. *Chem. Commun.* **48**(40), 4878 (2012).
69. D. Gu, W. Li, F. Wang, H. Bongard, B. Spliethoff, W. Schmidt, C. Weidenthaler, Y. Xia, D. Zhao, and F. Schuth: Controllable Synthesis of Mesoporous Peapod-like Co_3O_4@Carbon Nanotube Arrays for High-Performance Lithium-Ion Batteries. *Angew. Chem.* **54**(24), 7060 (2015).
70. Z. Bai, Z. Ju, C. Guo, Y. Qian, B. Tang, and S. Xiong: Direct large-scale synthesis of 3D hierarchical mesoporous NiO microspheres as high-performance anode materials for lithium ion batteries. *Nanoscale* **6**(6), 3268 (2014).
71. Y. Gong, M. Zhang, and G. Cao: Chemically anchored NiOx–carbon composite fibers for Li-ion batteries with long cycle-life and enhanced capacity. *RSC Adv.* **5**(34), 26521 (2015).
72. V. Aravindan, P. Suresh Kumar, J. Sundaramurthy, W.C. Ling, S. Ramakrishna, and S. Madhavi: Electrospun NiO nanofibers as high performance anode material for Li-ion batteries. *J. Power Sources* **227**, 284 (2013).
73. D. Xie, Q. Su, W. Yuan, Z. Dong, J. Zhang, and G. Du: Synthesis of Porous NiO-Wrapped Graphene Nanosheets and Their Improved Lithium Storage Properties *The Journal of Physical Chemistry C.* **117**(46), 24121 (2013).
74. Y.J. Mai, J.P. Tu, X.H. Xia, C.D. Gu, and X.L. Wang: Co-doped NiO nanoflake arrays toward superior anode materials for lithium ion batteries. *J. Power Sources* **196**(15), 6388 (2011).
75. D. Xie, W. Yuan, Z. Dong, Q. Su, J. Zhang, and G. Du: Facile synthesis of porous NiO hollow microspheres and its electrochemical lithium-storage performance. *Electrochim. Acta* **92**, 87 (2013).
76. X. Leng, S. Wei, Z. Jiang, J. Lian, G. Wang, and Q. Jiang: Carbon-Encapsulated Co_3O_4 Nanoparticles as Anode Materials with Super Lithium Storage Performance. *Sci. Rep.* **5**, 16629 (2015).
77. Y. Li, B. Tan, and Y. Wu: Mesoporous CO_3O_4 nanowire arrays for lithium ion batteries with high capacity and rate capability. *Nano Lett.* **8**(1), 265 (2008).
78. L. Li, G. Zhou, X-Y. Shan, S. Pei, F. Li, and H-M. Cheng: Co_3O_4 mesoporous nanostructures@graphene membrane as an integrated anode for long-life lithium-ion batteries. *J. Power Sources* **255**, 52 (2014).
79. R. Wang, C. Xu, J. Sun, L. Gao, and C. Lin: Flexible free-standing hollow Fe_3O_4/graphene hybrid films for lithium-ion batteries *J. Mater. Chem. A* **1**(5), 1794 (2013).
80. B.G. Choi, S.J. Chang, Y.B. Lee, J.S. Bae, H.J. Kim, and Y.S. Huh: 3D heterostructured architectures of Co_3O_4 nanoparticles deposited on porous graphene surfaces for high performance of lithium ion batteries. *Nanoscale* **4**(19), 5924 (2012).
81. X.N. Leng, S.F. Wei, Z.H. Jiang, J.S. Lian, G.Y. Wang, and Q. Jiang: Carbon-Encapsulated Co_3O_4 Nanoparticles as Anode Materials with Super Lithium Storage Performance. *Sci. Rep.* **5**, 11 (2015).
82. D. Chakraborty and G.N. Patey: Evidence that crystal nucleation in aqueous NaCl solution Occurs by the two-step mechanism. *Chem. Phys. Lett.* **587**, 25 (2013).
83. D. Chakraborty and G.N. Patey: How Crystals Nucleate and Grow in Aqueous NaCl Solution. *J. Phys. Chem. Lett.* **4**(4), 573 (2013).
84. B. Wang, X.L. Li, X.F. Zhang, B.J. Luo, M.H. Jin, M.H. Liang, S.A. Dayeh, S.T. Picraux, and L.J. Zhi: Adaptable Silicon–Carbon Nanocables Sandwiched between Reduced Graphene Oxide Sheets as Lithium Ion Battery Anodes. *ACS Nano* **7**, 1437 (2013).
85. L. Wang, Y. Zheng, X. Wang, S. Chen, F. Xu, L. Zuo, J. Wu, L. Sun, Z. Li, H. Hou, and Y. Song: Nitrogen-doped porous carbon/Co_3O_4 nanocomposites as anode materials for lithium-ion batteries. *ACS Appl. Mater. Interfaces* **6**(10), 7117 (2014).
86. X. Ge, C.D. Gu, X.L. Wang, and J.P. Tu: Correlation between Microstructure and Electrochemical Behavior of the Mesoporous Co_3O_4 Sheet and Its Ionothermal Synthesized Hydrotalcite-like α-$Co(OH)_2$ Precursor. *J. Phys. Chem. C* **118**(2), 911 (2014).
87. S. Xiong, J.S. Chen, X.W. Lou, and H.C. Zeng: Mesoporous Co_3O_4 and CoO@C Topotactically Transformed from Chrysanthemum-like $Co(CO_3)_{0.5}(OH)\cdot_{0.11}H_2O$ and Their Lithium-Storage Properties. *Adv. Funct. Mater.* **22**(4), 861 (2012).
88. C. Hou, X.Y. Lang, G.F. Han, Y.Q. Li, L. Zhao, Z. Wen, Y.F. Zhu, M. Zhao, J.C. Li, J.S. Lian, and Q. Jiang: Integrated solid/nanoporous copper/oxide hybrid bulk electrodes for high-performance lithium-ion batteries. *Sci. Rep.* **3**, 2878 (2013).
89. X.L. Jia, Z. Chen, X. Cui, Y.T. Peng, X.L. Wang, G. Wang, F. Wei, and Y.F. Lu: Building Robust Architectures of Carbon and Metal Oxide Nanocrystals toward High-Performance Anodes for Lithium-Ion Batteries. *ACS Nano* **6**, 9911 (2012).
90. C. Liang, D. Cheng, S. Ding, P. Zhao, M. Zhao, X. Song, and F. Wang: The structure dependent electrochemical performance of porous Co_3O_4 nanoplates as anode materials for lithium-ion batteries. *J. Power Sources* **251**, 351 (2014).
91. P. Poizot, S. Laruelle, S.D. Grugeon, L. Dupont, and J.M. Tarascon: Nano-sizedtransition-metaloxidesas negative-electrode materials for lithium-ion batteries. *Nature* **407**, 496 (2000).
92. C. He, S. Wu, N. Zhao, C. Shi, E. Liu, and J. Li: Carbon-Encapsulated Fe_3O_4 Nanoparticles as a High-Rate LithiumIon Battery Anode Material. *ACS Nano* **7**, 4459 (2013).
93. J. Zhu, L. Bai, Y. Sun, X. Zhang, Q. Li, B. Cao, W. Yan, and Y. Xie: Topochemical transformation route to atomically thick Co_3O_4 nanosheets realizing enhanced lithium storage performance. *Nanoscale* **5**(12), 5241 (2013).
94. L. Chen, Z. Wang, C. He, N. Zhao, C. Shi, E. Liu, and J. Li: Porous graphitic carbon nanosheets as a high-rate anode material for lithium-ion batteries. *ACS Appl. Mater. Interfaces* **5**(19), 9537 (2013).